

2016

Loop Current Eddy Formation and Baroclinic Instability

Kathleen A. Donohue

University of Rhode Island, kdonohue@uri.edu

D. R. Watts

University of Rhode Island

P. Hamilton

R. Leben

M. Kennelly

University of Rhode Island

Follow this and additional works at: <https://digitalcommons.uri.edu/gsofacpubs>

Citation/Publisher Attribution

Donohue, K., Watts, D.R., Hamilton, P., Leben, R., & Kennelly, M. (2016). Loop Current Eddy Formation and Baroclinic Instability. *Dynamics of Atmospheres and Oceans*, 76(2), 195-216.

Available at: <http://dx.doi.org/10.1016/j.dynatmoce.2016.01.004>

This Article is brought to you by the University of Rhode Island. It has been accepted for inclusion in Graduate School of Oceanography Faculty Publications by an authorized administrator of DigitalCommons@URI. For more information, please contact digitalcommons-group@uri.edu. For permission to reuse copyrighted content, contact the author directly.

Loop Current Eddy Formation and Baroclinic Instability

The University of Rhode Island Faculty have made this article openly available.
Please let us know how Open Access to this research benefits you.

This is a pre-publication author manuscript of the final, published article.

Terms of Use

This article is made available under the terms and conditions applicable towards Open Access Policy Articles, as set forth in our [Terms of Use](#).

Loop Current Eddy Formation and Baroclinic Instability

K.A. Donohue^{a,*}, D.R. Watts^a, P. Hamilton^b, R. Leben^c, M. Kennelly^a

^a*Graduate School of Oceanography, University of Rhode Island, Narragansett, Rhode Island USA*

^b*Leidos Inc. Raleigh, North Carolina, USA.*

^c*Department of Aerospace Engineering Sciences, University of Colorado Boulder, Boulder, Colorado, USA.*

Abstract

The formation of three Loop Current Eddies, Ekman, Franklin, and Hadal, during the period April 2009 through November 2011 was observed by an array of moored current meters and bottom mounted pressure equipped inverted echo sounders. The array design, areal extent nominally 89°W to 85°W, 25°N to 27°N with 30-50 km mesoscale resolution, permits quantitative mapping of the regional circulation at all depths. During Loop Current Eddy detachment and formation events, a marked increase in deep eddy kinetic energy occurs coincident with the growth of a large-scale meander along the northern and eastern parts of the Loop Current. Deep eddies develop in a pattern where the deep fields were offset and leading upper meanders consistent with developing baroclinic instability. The interaction between the upper and deep fields is quantified by evaluating the mean eddy potential energy budget. Largest down-gradient heat fluxes are found along the eastern side

*Corresponding author

Email address: `kdonohue@uri.edu` (K.A. Donohue)

of the Loop Current. Where strong, the horizontal down-gradient eddy heat flux (baroclinic conversion rate) nearly balances the vertical down-gradient eddy heat flux indicating that eddies extract available potential energy from the mean field and convert eddy potential energy to eddy kinetic energy.

Keywords:

Highlights:

- Large Loop Current meanders develop prior to separation as deep eddy energy grows
- A train of upper-deep eddy interactions leads to each Loop Current Eddy separation
- Deep eddies develop in a pattern consistent with baroclinic instability
- Mean eddy potential energy budget is evaluated with observations
- Horizontal downgradient eddy flux drives eddy kinetic energy

1 **1. Introduction**

2 The Loop Current (LC) dominates the circulation in the Gulf of Mexico.
3 As part of the North Atlantic western boundary current system, it enters the
4 Gulf through the Yucatan Channel and exits through the Straits of Florida.
5 While the shortest circuit within Gulf is a port-to-port mode along the north-
6 ern Cuban coast, the LC can penetrate the Gulf as far north as 28°N and as
7 far west as 93°W, expanding in area by a factor of 4 from the port-to-port
8 mode during its northward advancement (Leben, 2005). Its influence extends

9 to the far western Gulf due to the formation of large anticyclonic rings known
10 as Loop Current Eddies (LCE). On an irregular time interval a LCE pinches
11 off from the LC and migrates westward in the Gulf, the time interval between
12 separations can be as rapid as a few weeks or as long as 18 months (Vukovich
13 and Maul, 1985; Sturges and Leben, 2000; Leben, 2005). The LCE separation
14 process is not readily predictable, although an empirical linkage between re-
15 treat latitude and subsequent separation time has been found (Leben, 2005;
16 Alvera-Azcárate et al., 2009). Complex and multi-scale circulation is asso-
17 ciated with the LCE formation (Sturges and Leben, 2000). The separation
18 cycle often exhibits a series of detachments and reattachments before the
19 final separation (see, for example, the LCE Franklin formation discussed in
20 Liu et al. (2011b)). Frontal eddies and meanders along the periphery of the
21 LC are present during separation (Cochrane, 1972; Vukovich and Maul, 1985;
22 Fratantoni et al., 1998; Zavala-Hidalgo et al., 2003). The LC's influence ex-
23 tends beyond the depth of its surface-intensified core. Through interaction
24 with topography and LCE generation, the LC provides the primary forcing
25 of deep circulation. It has been hypothesized that deep energy generated
26 beneath the LC during LCE separation radiates away from its source to the
27 Gulf's boundary either as linear waves or eddies (Hamilton, 2009). At the
28 boundary, steep escarpments act to focus this deep energy into narrow swift
29 boundary currents (Oey and Lee, 2002; Oey, 2008).

30 Although qualitative analysis of surface fields has led to a classification
31 of separation modes based upon the juxtaposition of cyclonic eddies and LC
32 position within the Gulf (Schmitz, 2005), to date no theoretical framework
33 fully explains LCE formation. Pichevin and Nof (1997) and Nof and Pichevin

34 (2001) show that in order to conserve momentum, an anticyclonic eddy forms
35 as the northward flowing LC turns eastward and realistic numerical mod-
36 els have demonstrated this process (Chérubin et al., 2005; Chang and Oey,
37 2011). Numerical studies highlight the role of instability and LC-topographic
38 interactions in LCE formation e.g. Hurlburt and Thompson (1980); Hurlburt
39 (1986); Welsh and Inoue (2000); Oey (2008); Chérubin et al. (2006); Le Hénaff
40 et al. (2012). Essential in these studies are the feedbacks between upper and
41 deep circulation. Hurlburt (1986) and Oey (2008) suggested that the region
42 north of Campeche Bank is an important area for generation of deep eddies.
43 Large mean-to-eddy energy conversion rates appear along the western edge
44 of the Loop Current as the current moves off the relatively shallow western
45 slope of the Yucatan Channel into the deep topography of the Gulf. Eddies
46 propagate upstream along the Loop Current, grow in strength off the west
47 Florida Slope and participate in the LC’s necking-down that precedes LCE
48 separation (Oey, 2008). In the Gulf of Mexico literature “necking-down” is
49 often used to describe the spatial configuration where one or more adjacent
50 LC cyclones appear to pinch together the sides of an extended LC below
51 a developing LCE giving the LC a neck-like feature, e.g. Schmitz (2005).
52 Chérubin et al. (2005) showed that a baroclinically unstable vortex generates
53 a vigorous deep eddy field whose interaction with the LC becomes increas-
54 ingly complex when realistic Gulf topography is included. More recently, the
55 simulations in Le Hénaff et al. (2012) show that as frontal cyclones propa-
56 gate over the Mississippi Fan, a coupled upper-deep cyclone pair develops
57 that ultimately facilitates the LCE shedding process. Several studies have
58 suggested linkage between the passage of cyclonic eddies from the Caribbean

59 through Yucatan Channel to subsequent LCE separation (Oey et al., 2003;
60 Oey, 2004; Athié et al., 2012; Huang et al., 2013).

61 To address the need for full-water column observations during the full
62 eddy shedding cycle in order to improve the dynamical understanding of how
63 the LC interacts with and drives deep circulation, an array of twenty-five in-
64 verted echo sounders with pressure gauges (PIES), nine full-depth moorings
65 and seven near-bottom moorings was deployed April 2009 and recovered in
66 October-November 2011 as part of the Dynamics of the Loop Current in US
67 Waters Study (Figure 1). Three LCEs formed during the 30-month deploy-
68 ment, Ekman, Franklin, and Hadal (Figure 2). The array spanned 89°W
69 to 85°W, 25°N to 27°N with 30-50 km mesoscale resolution. This permits
70 quantitative mapping of the regional circulation during the LCE separation
71 events. Hamilton et al. (2015), this volume, provides a review of the ex-
72 periment and Hamilton et al. (2014) gives a detailed description of the field
73 operations and data processing.

74 We note that the *Deepwater Horizon* oil-spill event occurred in spring-
75 summer 2010 and coincided in time with Eddy Franklin’s formation. (The
76 *Deepwater Horizon* platform, 88.39°N, 28.74°N, was located well to the north,
77 230 km from the northwesternmost edge of the array discussed in this work.)
78 Considerable efforts were made during that time period to rapidly acquire and
79 analyze oceanographic observations as well to focus and improve modeling
80 studies. A thorough review of the subsequent literature is beyond the scope
81 of this study, as a starting point, the reader is referred to the dedicated
82 monograph, ‘Monitoring and Modeling the *Deepwater Horizon* Oil Spill: A
83 Record-Breaking Enterprise’ (Liu et al., 2011a) which provides a thorough

84 synopsis of those initial efforts and in particular the studies of Walker et al.
85 (2011); Liu et al. (2011b); Shay et al. (2011); Hamilton et al. (2011) which
86 focus on large and meso-scale circulation in spring-summer 2010.

87 This paper focuses upon the coupling between the upper and deep circula-
88 tion during LCE formation. We describe the data set in Section 2, statistics
89 related to the deep circulation are provided in Section 3; case studies of
90 upper-deep coupling for the three eddy events are shown Section 4; the mean
91 potential energy budget is diagnosed in Section 5, and the paper concludes
92 with a discussion and conclusion in Sections 6 and 7.

93 **2. Data**

94 The observational array consists of nine tall moorings, seven short moor-
95 ings and twenty-five PIES. The suite of instrumentation on the tall moor-
96 ings includes an upward-looking 75-kHz acoustic Doppler current profiler at
97 450 m depth and point current meters at 600, 900, 1300, 2000 m depth and
98 100 m above the bottom as well as temperature recorders placed at 75, 150,
99 250, 350, 525, 750, 1100, 1500 m depth. Short moorings have one current
100 meter positioned 100 m above the bottom. The PIES, moored at the sea
101 floor, emits 12 kHz sound pulses and measures the round trip acoustic travel
102 times, τ , of these acoustic pulses from sea floor to sea surface, and a pressure
103 gauge contained within the instrument's housing measures bottom pressure.
104 Sampling frequency from the multiple sensors varies from minutes to hours.
105 Here we utilize time series that have been 72-hour low pass filtered with a
106 fourth order Butterworth filter and subsampled at 12-hour intervals. The
107 Loop Current Study had excellent data return: 100% PIES and 94% tall

108 and short moorings. A detailed description of instrumentation and standard
109 processing is provided in Hamilton et al. (2014).

110 Using empirically-derived look-up tables between τ and historical hydrog-
111 raphy (a so-called GEM field, Meinen and Watts (2000)), vertical profiles of
112 temperature, salinity, and density are estimated. Hamilton et al. (2014) and
113 Donohue et al. (2015) discuss specific treatment of this methodology to the
114 Gulf. Application of objective analysis yields 4-dimensional maps of temper-
115 ature, salinity, density, and geostrophic streamfunction at 12-hour intervals.
116 An example of the mapped products for June 24, 2009 is shown in Figure 3.
117 The vector sums of mapped baroclinic velocity profiles (geostrophic velocities
118 referenced to zero at 3000 dbar, subscript *bc*) plus deep reference velocities
119 (subscript *ref*) give the estimated absolute geostrophic velocities throughout
120 the water column. Absolute sea surface heights, SSH, are also determined.
121 First, 3000-dbar pressures are converted to their height equivalent (leveled
122 pressure anomaly divided by gravity and density). We term this component
123 the reference level sea surface height (SSH_{ref}). Second, surface geopotentials
124 referenced to 3000 dbar are converted to their height equivalent (geopotential
125 divided by gravity). Geopotential height is estimated from the GEM fields
126 combined with measured τ . We term this component the baroclinic SSH
127 referenced to the bottom (SSH_{bc}). The *bc* and the *ref* contributions to sea
128 surface height are combined to yield absolute sea surface height. Equations
129 1-3 summarize the SSH calculation,

$$SSH_{ref} = \frac{p_{ref}}{\rho_b g}, \quad (1)$$

$$SSH_{bc} = \frac{\phi_{bc}}{g}, \quad (2)$$

$$\text{SSH}_{abs} = \text{SSH}_{ref} + \text{SSH}_{bcb}, \quad (3)$$

130 where g is gravity, ρ_b is mean bottom density, ϕ_{bcb} is geopotential referenced
 131 to 3000 dbar, and p_{ref} are the 3000-dbar pressures. This decomposition
 132 of SSH has been successfully applied with PIES in other strong western
 133 boundary current systems such as the Agulhas (Baker-Yeboah et al., 2009),
 134 the Kuroshio Extension (Park et al., 2012), and the Antarctic Circumpolar
 135 Current (Behnisch et al., 2013).

136 Extensive intercomparison between mapped fields and point measure-
 137 ments indicates that the PIES methodology works well in this region. Details
 138 and comparison figures are provided in Hamilton et al. (2014) and Donohue
 139 et al. (2015), this volume. Briefly, temperature comparisons, for the nine
 140 tall moorings at 9 depth levels reveal correlation coefficients greater than
 141 0.92 at all depths, and greater than 0.975 at all sites for depths between 250
 142 and 750 m, indicating that the PIES capture more than 95% of variance.
 143 Rms differences are near 0.6°C at 250 m depth and decrease to 0.23°C at
 144 900 m depth. PIES-mapped currents were compared to mooring currents at
 145 six nominal depths. Correlation coefficients are above 0.89, especially within
 146 the thermocline. Rms differences are less than 10 cm s⁻¹ everywhere and de-
 147 crease to less than 5 cm s⁻¹ below 600 m depth. PIES SSH and along-track
 148 Jason-2 altimeter SSH also compare well, correlation coefficients are above
 149 0.95. Comparisons with along-track Jason-2 altimeter SSH anomaly confirm
 150 an estimated PIES SSH error of 5.7 cm.

151 To place the array in the larger regional context, we take advantage of
 152 mapped satellite altimeter data. LCE separation times and LC area as well
 153 as the mapped fields are determined from the Colorado Center for Atmo-

154 spheric Research (CCAR) Gulf of Mexico (GOM) objectively mapped his-
155 torical mesoscale altimeter data reanalysis. These products use the quick-
156 look mesoscale processing system (Leben et al., 2002) based on RADS 3.0
157 archive. Gridding uses a multigrid Cressman objective analysis of all avail-
158 able altimeter data. The satellite altimeter data used to produce the his-
159 torical reanalysis during the observational program include Jason-1, Envisat,
160 and OSTM/Jason-2. A detailed description of the processing of the GOM
161 SSH dataset can be found in Hamilton et al. (2014). Detachment of LCEs
162 from the LC is identified by the breaking of the 17-cm SSH contour in the
163 CCAR GOM historical SSH data product. In this product, the 17-cm SSH
164 contour closely tracks the core of the LC that enters through the Yucatan
165 Channel and exits through the Florida Straits (Leben, 2005). Dukhovskoy
166 et al. (2015) provides an evaluation of the tracking technique.

167 **3. Deep statistics**

168 In contrast to the broad anticyclonic mean flow observed in the upper
169 ocean (Figure 4a), the mean deep circulation exhibits more structure (Figure
170 4b). Along the western side of the array, a deep mean anticyclonic gyre with
171 ~ 200 km lateral extent is centered near 26.3°N 87.3°W with mean speeds
172 near 6 cm s^{-1} . In the east, there is a deep mean cyclonic gyre positioned
173 near 26.2°N 85.7°W with speeds near 3 cm s^{-1} . Along the southern boundary
174 of the array, mean deep flow is to the north and west. Standard deviation
175 ellipses are mainly isotropic except at the mooring closest to the west Florida
176 Shelf where the ellipse is elongated and parallel to the slope. Elevated time-
177 mean eddy kinetic energy (EKE) is found beneath the mean position of the

178 LC. This swath of high EKE can be traced from the Mississippi Fan, where
179 it is offset slightly to the north of the mean LC position, across the array
180 to the southeast, where the EKE maximum lies slightly west of the mean
181 LC. Array-averaged EKE shows the influence of the LC (Figure 4, panels
182 c,d). Enhanced EKE occurs during LCE shedding events. During Ekman,
183 Franklin, and Hadal, peak EKE occurs at or near the first eddy detachment.
184 An additional EKE peak occurs in June 2011, during this time, the LC necks
185 down but does not form an eddy. During LC eddy detachment and formation
186 events, a marked increase in deep eddy kinetic energy occurs (Figures 4d)
187 coincident with the development of a large-scale meander along the northern
188 and eastern parts of the LC (Figure 2).

189 Mesoscale variance distribution as a function of frequency also differs be-
190 tween the upper and deep ocean. The discussion will treat variance whereas
191 Figure 5 displays standard deviation. Note the range choices for the fre-
192 quency bands shown in Figure 5 are based upon spectral peaks shown in
193 Figure 6. Upper-ocean variance is dominated by the low-frequency lateral
194 movement of the LC in and out of the array during LC eddy shedding cycles,
195 and only 14% of the variance is in periods shorter than 100 days (Dono-
196 hue et al., 2015). There is proportionally more deep variance in the high-
197 frequency bands (Figure 5): 72 % of the deep variance is in periods shorter
198 than 100 days. Within the 100- to 3-day mesoscale band, deep variance is
199 distributed as follows: 57% within 100 to 40 day, 30% within 40 to 20 day,
200 13% within 20 to 3 day. Similar to the upper ocean, the spatial structure
201 of the deep variance changes as a function of frequency band (Figure 5).
202 Within the highest frequency band, 20 to 3 days, elevated values occur along

203 the base of the Mississippi Fan in the northwest portion of the array. As
204 frequency decreases, this ridge of high variance shifts to the southeast within
205 the array. In the lowest frequency band, 100 to 40 days, the spatial pattern
206 resembles the time-mean EKE (Figure 4).

207 A signature of growing baroclinic instability events is a vertical phase
208 tilt: along the direction of propagation, with deep fields leading upper fields.
209 Consequently, at a fixed location, deep leads upper in time also. To in-
210 vestigate vertical coupling, the coherences and phases between upper and
211 deep streamfunctions (SSH_{bc} and SSH_{ref} , respectively) are estimated using
212 the averaged periodogram method of Welch (1967) (256-day length segment
213 with 50% overlap). Upper and deep streamfunctions are coherent over large
214 portions of the array for frequencies between $1/64 \text{ d}^{-1}$ and $1/32 \text{ d}^{-1}$. Fig-
215 ure 7 shows the spatial pattern of coherence and phase for three frequencies
216 within this band. A tongue of high coherence extends from the northeast
217 trending south-southwest toward the central portion of the array where the
218 three LCE's separated. Two additional peaks occur, one near the base of
219 the Mississippi Fan and another in the southeastern corner. Where statisti-
220 cally coherent, the phase offset is such that the deep leads the upper. Phase
221 estimates range between 60 and 150 degrees. Frequencies outside the band
222 $1/64 \text{ d}^{-1}$ and $1/32 \text{ d}^{-1}$ do not show statistically significant coherence between
223 upper and deep.

224 4. Case Studies

225 The preceding spectral approach characterizes the overall mean statistics,
226 yet each LC eddy shedding event is unique, e.g., location of final separation,

227 number of brief detachments that precede the separation, location of the LC
228 regarding bottom topography and what portion was mapped by the array
229 (Figure 2). To illustrate the evolution of LC eddy-shedding events and the
230 relationship between upper and deep, maps of upper and deep streamfunc-
231 tion are plotted at short time intervals (four-to-five days). In each case study,
232 mapped baroclinic SSH referenced to the bottom (SSH_{bc} , filled colored con-
233 tours) is embedded within altimetric SSH that covers the broader region. The
234 17-cm contour denotes the location of the LC and LC-eddy fronts. Mapped
235 SSH_{ref} reveals the presence of deep cyclones (blue contours) and deep anti-
236 cyclones (red contours). Two sets are provided for each shedding event: full
237 frequency (3-day low-pass), and 100 to 40-day band pass fields (Figures 8 - 9
238 for Ekman, Figures 10 - 11 for Franklin and Figures 12 - 13 for Hadal). The
239 following discussion focuses upon the 100 to 40 day band in which coherence
240 between upper and deep is found to be high.

241 *Eddy Ekman: 4 May to 4 October 2009.* A long-wavelength meander devel-
242 ops along the northern edge of the LC in early July (Figure 8). Perturbations
243 in the deep field begin to appear in early May and intensify in late July. The
244 4 July map depicts two deep eddies labeled as cyclone A and anticyclone
245 B (Figure 9). These two deep eddies are positioned on this date such that
246 the deep anticyclone B leads an upper high, and the deep cyclone A slightly
247 leads an upper low. This classic pattern associated with baroclinic instabil-
248 ity remains with varying vertical phase-tilt as the meander and deep eddies
249 propagate together anticyclonically along the LC periphery from 4 July to
250 25 August. While the amplitude of deep cyclone A remains nearly constant
251 during this interval, deep anticyclone B's strength modulates. Anticyclone

252 B intensifies from 8 to 20 July, remains constant in strength until 28 July,
253 then weakens over the next 10 days. A slight re-amplification occurs 25 Au-
254 gust. On 24 July (Figure 9), another deep cyclone labeled C, located on the
255 Mississippi Fan, begins to develop. It is positioned slightly downstream of a
256 developing upper trough. This trough and deep cyclone C jointly intensify 24
257 July through 21 August. During this interval, the trough deepens to nearly
258 pinch off the neck of the LC, and the vertical phase tilt gets smaller as deep
259 cyclone C becomes nearly vertically aligned under the trough. By 29 August,
260 the phasing of deep leading upper no longer exists, Eddy Ekman is nearly
261 separated, and deep cyclone C has weakened and subsequently propagates
262 southwestward out of the array.

263 *Eddy Franklin: 11 April to 13 September 2010.* Similar to Eddy Ekman,
264 during the formation of Eddy Franklin, the signature vertical phase tilts of
265 baroclinic instability are present. This case study includes upper and deep
266 events leading to an eddy detachment in early July 2010 and final separation
267 in early August 2010 (Figure 10). Consider the large-scale LC meander that
268 is developing in early May 2010. The 11 May map (Figure 11) shows two
269 deep eddies, anticyclone A and cyclone B. They are positioned such that the
270 deep anticyclone resides downstream of and leads the upper crest. The deep
271 cyclone B resides upstream of that upper crest, and in subsequent days (5
272 June to 25 June) cyclone B intensifies as it leads a developing upper trough
273 within the array. Anticyclone C comes into view 5 June with an upper
274 crest following close behind it. During June, the B and C deep eddies and
275 their slightly trailing upper meander trough and crest propagate downstream
276 around the Loop. The trough and deep eddy B jointly intensify, and by early

277 July (Figure 11) the LC neck pinches off into a short-lived detachment. The
278 30 June map shows three deep eddies; a deep cyclone, labeled D, appears
279 near the Mississippi Fan. The northern limit of the array leaves the question
280 open as to whether these deep eddies (A, B, C or D) initially propagate
281 into the array from further north, or whether they originate upstream along
282 the LC front. During July, deep eddies C and D and their slightly trailing
283 upper meander crest and trough propagate downstream around the LC. For
284 example, on 10 and 15 July 2010, the vertical phase tilt is evident, and
285 the features jointly intensify. Eventually, the trough ‘necks down’ again,
286 and eddy separation occurs in August. The recurrent structure observed
287 in these map sequences is that as deep eddies propagate through the array
288 they lead their upper counterpart and this leads to joint amplification. For
289 example, from 5 June to 10 July (Figure 11), deep cyclone B leads an upper
290 cyclone (trough); from 15 July to 4 August, deep anticyclone C leads an upper
291 anticyclone. Finally, we note that during the Franklin event, the largest
292 amplitude deep eddies occur during the early to mid-July detachment, prior
293 to the final separation of a relatively small LC eddy in August.

294 *Eddy Hadal: 9 March to 11 August 2011.* Upper-deep coupling with the ver-
295 tical phase tilt of baroclinic instability also characterizes the Hadal shedding
296 cycle. Figure 12, shows that during Hadal, long-wavelength meanders de-
297 velop along the eastern side of an extended LC. The eastern side of the LC
298 runs through the middle of the array during much of this time, and the associ-
299 ated deep eddies are relatively well centered within the observational window.
300 This case study will follow a sequence of four deep eddies, anticyclones A and
301 C, and cyclones B and D (Figure 13). As seen in our Ekman and Franklin

302 case studies, while these deep eddies translate along the LC, they lead their
303 upper counterpart as they jointly develop and tend to constrict the neck. For
304 example, on 13 April, deep anticyclone A sits just downstream of an upper
305 crest (high SSH_{bc}), and during the subsequent 15 days the upper and deep
306 highs jointly intensify. Shortly after that, on 3 May deep cyclone B leads an
307 upper trough (low SSH_{bc}), and both intensify during the subsequent 20 days.
308 Immediately following that, on 23 May, the deep anticyclone C leads an up-
309 per crest downstream, intensifying during the next 20-30 days to about 22
310 June. Deep-cyclone D follows this train of upper-deep coupling interactions.
311 From 22 June to 17 July 2011 deep-cyclone D leads and jointly develops with
312 an upper low SSH_{bc} and trough, constricting the LC neck greatly. Shortly
313 afterward Hadal separates. Limits to the growth phase of the upper and
314 deep perturbations appear to occur when the deep eddy trajectory turns to
315 the southwest, not following the downstream path of the upper jet. Subse-
316 quently, their vertical phase tilt becomes non-conducive to baroclinic insta-
317 bility, and they jointly decay. Deep-cyclone B decays after 28 May together
318 with its upper-strong low. Analogously deep-anticyclone C decays after 22
319 June together with its upper strong high. Similar to the Franklin event, large
320 amplitude deep eddies and joint intensification (mid-April through late June)
321 occur prior to the final eddy separation (mid-August).

322 **5. Eddy Potential Energy**

323 The terms in the time-mean eddy potential-energy budget are evaluated
324 so as to diagnose the role of eddies in the system. The results below will
325 demonstrate that eddies extract potential energy from the mean field (stored

326 in the sloping isopycnals of the LC) and ultimately convert that energy to
 327 eddy kinetic energy.

328 Following Cronin and Watts (1996) and Bishop et al. (2013), a quasi-
 329 geostrophic framework (small Rossby number, β plane) is assumed to be valid
 330 for our diagnostics. Temperature will be a proxy for density: $\rho = \rho_o(1 - \alpha T)$,
 331 where α is an effective thermal expansion coefficient ($10^{-4} \text{ }^\circ\text{C}^{-1}$). Potential
 332 energy budget terms are evaluated near 400 m depth. This avoids the near-
 333 surface depth of subtropical underwater where the role of salinity would have
 334 to be independently included when calculating density.

335 In a Boussinesq incompressible fluid, the time-mean temperature equation
 336 can be written as:

$$\overline{\mathbf{u}} \cdot \nabla \overline{T} = -\overline{w}\theta_z - \nabla \cdot \overline{\mathbf{u}'T'}, \quad (4)$$

337 where $\mathbf{u} = (u, v)$ is geostrophic velocity, T is temperature, w is verti-
 338 cal velocity and θ_z is the regional background vertical temperature gradient.
 339 Overbars indicate a time mean and primes are the deviation from the mean.
 340 In the following discussion, $\mathbf{u}'T'$ is referred to as ‘heat flux’ since implicitly
 341 eddy temperature flux multiplied by density and specific heat at constant
 342 pressure ($\rho_o C_p$) is a heat flux. Equation 4 states that mean horizontal advec-
 343 tion is balanced by mean vertical advection and the divergence of horizontal
 344 eddy heat flux. Note that the dynamically important part of the eddy heat
 345 flux term is the divergent component of eddy heat flux.

346 Eddy heat flux can be decomposed into rotational and divergent compo-
 347 nents by Helmholtz’s theorem. The rotational component recirculates heat
 348 whereas the divergent component provides the net lateral heat flux that trans-

349 fers potential energy into eddies. It is a challenge, numerically and observa-
 350 tionally to isolate these divergent eddy heat fluxes from the total eddy heat
 351 flux (see Griesel et al. (2009) for a recent discussion).

352 The approach will be to take advantage of the vector decomposition,
 353 shown in Figure 3 and expressed as the baroclinic velocity relative to the
 354 bottom plus a bottom reference velocity, $\mathbf{u} = \mathbf{u}_{bcb} + \mathbf{u}_{ref}$. In strong advective
 355 systems, mean ψ_{bcb} streamlines are very nearly parallel to mean temperature
 356 contours and therefore do not advect mean temperature. Figure 14 shows
 357 the nearly linear relationship between mean ψ_{bcb} and mean T at 400 m within
 358 our array. Therefore

$$\mathbf{u}'_{bcb} \cdot \nabla T' = 0. \quad (5)$$

359 The divergent component of the heat flux arises from the nearly depth-
 360 uniform reference current, of which a component can cross the time-varying
 361 baroclinic LC front. The dynamically important divergent heat flux is en-
 362 tirely contained in $\mathbf{u}'_{ref}T'$. Figure 15 shows the mean eddy heat fluxes for
 363 the three LC eddy-shedding events superimposed on temperature variance.
 364 Eddy heat flux is calculated three ways for this illustration, using the total
 365 eddy velocity ($\mathbf{u}'T'$), baroclinic eddy velocity ($\mathbf{u}'_{bcb}T'$), and reference eddy
 366 velocity ($\mathbf{u}'_{ref}T'$). For each eddy event, $\mathbf{u}'T'$ has the largest magnitudes. As
 367 expected from Marshall and Shutts (1981) $\mathbf{u}'_{bcb}T'$ circulates around temper-
 368 ature variance illustrating its rotational non-divergent nature. $\mathbf{u}'_{ref}T'$ shows
 369 downgradient heat fluxes in all events with strongest fluxes along the eastern
 370 side of the LC where the strongest growth occurred.

371 The eddy potential energy budget in steady state is determined by mul-
 372 tiplying the temperature equation by $g\alpha T'/\theta_z$ and averaging,

$$0 = -\bar{\mathbf{u}} \cdot \nabla \frac{g\alpha}{2\theta_z} \overline{T'^2} - \nabla \cdot \overline{\mathbf{u}' \frac{g\alpha}{2\theta_z} T'^2} - \frac{g\alpha}{\theta_z} \overline{\mathbf{u}' T'} \cdot \nabla \bar{T} - g\alpha \overline{T' w'} \quad (6)$$

373 where eddy potential energy is defined as

$$EPE = \frac{g\alpha}{2\theta_z} \overline{T'^2}. \quad (7)$$

374 Dividing by $\alpha g/\theta_z$ and rearranging yields,

$$\underbrace{\bar{\mathbf{u}} \cdot \nabla \frac{1}{2} \overline{T'^2}}_{\text{MAP}} + \underbrace{\nabla \cdot \overline{\mathbf{u}' \frac{1}{2} T'^2}}_{\text{EAP}} + \underbrace{\theta_z \overline{T' w'}}_{\text{PKC}} = \underbrace{-\overline{\mathbf{u}' T'} \cdot \nabla \bar{T}}_{\text{BC}} \quad (8)$$

375 Equation 8 states that the horizontal down-gradient eddy heat flux (BC)
 376 is balanced by the mean advection of eddy potential energy (MAP), eddy
 377 advection of eddy potential energy (EAP) and the vertical down-gradient
 378 heat flux (PKC). In baroclinic instability, the eddy conversion term (BC)
 379 of mean potential energy to eddy potential energy is balanced by the eddy
 380 conversion of eddy potential to eddy kinetic energy (PKC).

381 If we decompose our velocity field as described above into the baroclinic-
 382 referenced-to-the-bottom and reference components, we can rewrite the eddy
 383 energy budget:

$$\begin{aligned} \bar{\mathbf{u}}_{bc} \cdot \nabla \frac{1}{2} \overline{T'^2} + \bar{\mathbf{u}}_{ref} \cdot \nabla \frac{1}{2} \overline{T'^2} + \nabla \cdot \overline{\mathbf{u}'_{bc} \frac{1}{2} T'^2} + \nabla \cdot \overline{\mathbf{u}'_{ref} \frac{1}{2} T'^2} + \theta_z \overline{T' w'} \\ = -\overline{\mathbf{u}'_{bc} T'} \cdot \nabla \bar{T} + -\overline{\mathbf{u}'_{ref} T'} \cdot \nabla \bar{T} \end{aligned} \quad (9)$$

384 Because the baroclinic-referenced-to-bottom velocities flow along mean
 385 temperature contours (Figure 15), there is a relationship between mean tem-
 386 perature and velocity (Marshall and Shutts, 1981):

$$f \bar{\mathbf{u}}_{bc} = 2\gamma \hat{\mathbf{k}} \times \nabla \bar{T} \quad (10)$$

387 where γ is an empirical constant,

$$\gamma = \frac{1}{2} \frac{d\psi_{bc}}{d\bar{T}}. \quad (11)$$

388 Cronin and Watts (1996) and Bishop et al. (2013) argue that instantaneous
389 field

$$f \mathbf{u}'_{bc} = 2\gamma \hat{\mathbf{k}} \times \nabla T' \quad (12)$$

390 also holds.

391 Equations 11 and 12 state that the baroclinic-referenced-to-the-bottom
392 field is aligned vertically with the front (“equivalent barotropic”), which is a
393 good approximation in our array (Figure 14). With this decomposition, the
394 following relationships hold:

$$\overline{\mathbf{u}_{bc}} \cdot \nabla \frac{1}{2} \overline{T'^2} = -\overline{\mathbf{u}'_{bc} T'} \cdot \nabla \bar{T} \quad (13)$$

395 and

$$\nabla \cdot \overline{\mathbf{u}'_{bc} \frac{1}{2} T'^2} = 0 \quad (14)$$

396 Therefore, the mean eddy potential energy budget can be reduced to the
397 following:

$$\underbrace{\overline{\mathbf{u}_{ref}} \cdot \nabla \frac{1}{2} \overline{T'^2}}_{\text{MAP}_{ref}} + \underbrace{\nabla \cdot \overline{\mathbf{u}'_{ref} \frac{1}{2} T'^2}}_{\text{EAP}_{ref}} + \underbrace{\overline{\theta_z T' w'}}_{\text{PKC}} = \underbrace{-\overline{\mathbf{u}'_{ref} T'}}_{\text{BC}_{ref}} \cdot \nabla \bar{T} \quad (15)$$

398 Hereafter the subscript *ref* will be dropped from Equation 15.

399 To calculate these terms, one needs to determine vertical velocity w and
400 mean θ_z . θ_z is determined by the mean stratification within the array and at
401 400 m depth has a value of 0.023 °C m⁻¹. Following Lindstrom and Watts

402 (1994) and Howden (2000), vertical velocity is estimated near the base of the
 403 thermocline from the depth of the 6° isotherm (Z_6)

$$w = \frac{\partial Z_6}{\partial t} + \mathbf{u} \cdot \nabla Z_6. \quad (16)$$

404 Z_6 is negative and becomes increasingly negative with depth.

405 Figures 16 through 21 in the following LCE-specific discussions show the
 406 results of calculating the terms in the mean eddy potential energy budget
 407 (Equation 15). The maps summarize the energy conversion rates over the
 408 time interval of each respective case study. It is beyond the scope of this
 409 work to try to close the energy budget. Rather the aim is to illustrate major
 410 process of energy conversion.

411 *Eddy Ekman.* The BC term closely balances the sum of the PKC, EAP and
 412 MAP terms (Figure 16). The BC term is positive (indicating down-gradient
 413 fluxes) along the northwestern corner near the Mississippi Fan and along the
 414 eastern side of the LC. Overall, the pattern in the PKC term corresponds well
 415 to the BC term, although their respective maxima and minima are slightly
 416 displaced. Time series of the BC' and PKC' terms in three regions where both
 417 terms are strong and positive are shown in Figure 17. Here BC' is defined
 418 as $-\mathbf{u}'_{ref} T' \cdot \nabla \bar{T}$ and PKC' is defined as $\theta_z T' w'$. Time series track each
 419 other well and are positively correlated with one another, with correlation
 420 coefficients (r) ranging from 0.51 to 0.74. The peaks in the time series can
 421 be traced back to dates when the deep eddies and upper SSH_{bc} 100-to-40
 422 day band passed fields jointly intensify (Figure 9). For the three time series
 423 shown here, located at the correspondingly color-coded stars on the map at
 424 the top of the figure, the peaks are associated with times when deep cyclone A

425 intensifies as it propagates along the LC periphery: near the Mississippi Fan
426 (magenta star in Figure 17) in mid-July, when deep anticyclone B intensifies
427 at the northeast corner (blue star) in late July and when deep cyclone C
428 intensifies in the southeast corner (cyan star) in early August.

429 *Eddy Franklin.* Similar to Ekman, during the Franklin event, the BC term
430 closely balances the sum of the PKC, EAP and MAP terms (Figure 18). The
431 BC term is positive (indicating down-gradient fluxes) near the base of the
432 Mississippi Fan, along the eastern side of the LC as well as in the central
433 portion of the array. Overall, the pattern in the PKC term corresponds well to
434 the BC term, although the maxima and minima are again slightly displaced
435 from one another. Additionally, the range of PKC values is larger than
436 the BC range, particularly in the central array. Time series of the BC' and
437 PKC' terms in three regions where both terms are strong and positive are
438 shown in Figure 19. Note the vertical scale extends to higher rates than
439 for the other two eddy separation case studies discussed here. Time series
440 track each other well and are positively correlated with one another, with
441 correlation coefficients (r) ranging from 0.49 to 0.67. Positive BC and PKC
442 peaks along the eastern side of the LC coincide with the propagation and
443 development of several deep eddies. In the southeast (magenta star in Figure
444 19), peaks are due to the intensification of deep anticyclone A (Figure 11)
445 in early May. Along the northeast (blue star in Figure 19) the peak is due
446 to the intensification of deep cyclone B. In the central array (cyan star), the
447 late-June BC and PKC peaks occur when deep anticyclone C intensifies.

448 *Eddy Hadal.* Just as for the Ekman and Franklin case studies, the BC term
449 nearly balances the sum of the PKC, EAP and MAP terms (Figure 20). The

450 BC term has a maximum just downstream of the Mississippi Fan near 26.2°N ,
451 86.2°W . The PKC term is also high here, indicating that eddies gain potential
452 energy from the mean LC and convert that energy to eddy kinetic energy.
453 An additional maximum occurs in the PKC field, near 26.2°N , 87.5°W , and
454 here the balance is mainly between PKC and EAP. Figure 21 shows the
455 time series of BC' and PKC' centered on a location where both terms sum
456 to a strong positive peak. Again, the time series track each other well; the
457 correlation coefficient is 0.86. The two large peaks in the time series, late
458 April and mid-May, coincide with the intensification of deep cyclone B and
459 deep anticyclone C, respectively (Figure 13).

460 **6. Discussion**

461 These observations, resolving the full-water column mesoscale circulation,
462 provide a new perspective on LCE detachment and separation. The ‘necking
463 down’ of the LC is achieved through the amplification of the meander trough
464 that extends across the LC. It is a full water-column process. During the LCE
465 detachment and formation events, a marked increase in deep eddy kinetic
466 energy occurs coincident with the growth of a large-scale meander along the
467 northern and eastern parts of the LC. The trough deepens through a train of
468 upper-deep eddy interactions that precede each separation. Strongest upper-
469 deep interaction and the most energetic deep eddies can occur well in advance
470 of the final eddy separation. Joint intensification is intermittent, lasting only
471 tens of days while the vertical phase tilt is optimal for baroclinic growth.
472 Topography allows the deep eddies to propagate across the neck between
473 the base of the Mississippi Fan and the Campeche Bank to effectuate LCE

474 detachment and separation.

475 A preferred time-scale for upper-deep coupling emerges. Upper and deep
476 stream function are coherent within the frequency band between 100 and
477 40 d, the spatial offset is one where, in the direction of propagation, deep
478 leads upper. Donohue et al. (2015) and Hamilton et al. (2015), this issue,
479 show that these fluctuations cannot be traced back to Yucatan Channel.
480 This contrasts the historical view that it is the downstream growth of LC
481 peripheral frontal eddies that leads to LCE formation. Due to the limited
482 spatial domain of the array, we cannot identify the trigger mechanism. In
483 other words, we cannot unambiguously distinguish between locally generated
484 deep eddies and external deep eddies that may enter and intensify when they
485 encounter favorable phasing with the upper thermocline waters. Peripheral
486 eddies may yet play an important role in LCE formation. The modeling
487 study of Le Hénaff et al. (2012) suggests that as upper layer frontal cyclones
488 propagate over the Mississippi Fan, a deep cyclone is generated. In their
489 simulation, the upper-deep pair is shown to propagate across the LC and
490 facilitate LCE formation. Recent modeling efforts, (Chérubin et al., 2006;
491 Oey, 2008) explore how the position of the LC relative to topography plays a
492 role in the stability of the current, with particular focus on circulation near
493 Campeche Bank and the western side of the LC. Results from this study
494 instead highlight the importance of the northeast corner of the LC where
495 rapid growth of LC meanders and generation of strong deep EKE occur.

496 The energetics for the three shedding events share the following charac-
497 teristics. First, the magnitude of eddy advection of eddy potential energy,
498 EAP, a triple-correlation term which has often been assumed small, must

499 in fact be included in the budget, because it is of the same order as the
500 baroclinic conversion (BC) and vertical down-gradient heat flux (PKC). The
501 mean advection of eddy potential energy (MAP) by the *ref* field is small
502 compared to the other four terms. The spatial pattern and magnitude of the
503 combined PKC+EAP+MAP terms are very similar to the BC term. Second,
504 at any particular location, the time series that contribute to the terms in the
505 eddy energy budget are episodic in the LC, often with only a few events dom-
506 inating the mean. Conversion of available potential energy to eddy kinetic
507 energy occurs primarily along the eastern edge of the LC.

508 **7. Conclusion**

509 Deep eddies that occur during and near Loop Current Eddy detachment
510 gain their high-energy levels in a pattern consistent with developing baro-
511 clinic instability. The periodicities associated with these are 100 to 40-days.
512 Coherence estimates and case studies reveal that the deep streamfunction
513 perturbations lead corresponding perturbations in the upper streamfunction,
514 as they jointly intensify during a train of 3-4 cyclone/anticyclone pairs. This
515 baroclinic instability is intrinsically a whole-water-column process, and the
516 interaction between the upper and lower water column is quantified by eval-
517 uating the mean-eddy potential-energy budget. The baroclinic energy con-
518 version term, represented by down-gradient eddy heat fluxes, is found to be
519 largest along the eastern side of the LC. In these peak conversion regions
520 there is a near balance between horizontal down-gradient eddy heat fluxes
521 (baroclinic conversion rate) and vertical down-gradient eddy heat fluxes, indi-
522 cating that eddies extract available potential energy from the mean baroclinic

523 field and further convert that eddy potential energy to eddy kinetic energy.

524 **8. Acknowledgments**

525 The principal authors were supported by the Bureau of Ocean Energy
526 Management (BOEM) through contract M08PC20043 with Leidos, Inc. (for-
527 merly Science Applications International Corporation, SAIC). The authors
528 wish to thank Alexis Lugo-Fernandez, the contracting officer’s representative
529 for his enthusiastic support. The successful deployment and recovery of the
530 array was due to the instrument development and careful preparation and
531 planning by James Singer, Paul Blankinship, Erran Sousa, Stuart Bishop,
532 Brian Roderick, Gary Savoie and Cathy Cippolla. R. Leben acknowledges
533 support from BOEM contracts M08PC20043 and M10PC00112 to Leidos
534 Corporation, and NASA Ocean Surface Topography Mission Science Team
535 Grants NNX08AR60G and NNX13AH05G.

536 Alvera-Azcárate, A., Barth, A., Weisberg, R. H., 2009. The surface circula-
537 tion of the Caribbean Sea and the Gulf of Mexico as inferred from satellite
538 altimetry. *J. Phys. Oceanogr.* 39 (3), 640–657.

539 Athié, G., Candela, J., Ochoa, J., Sheinbaum, J., 2012. Impact of Caribbean
540 cyclones on the detachment of Loop Current anticyclones. *J. Geophys. Res.*
541 117 (C3), C03018.

542 Baker-Yeboah, S., Watts, D. R., Byrne, D. A., 2009. Measurements of sea sur-
543 face height variability in the eastern South Atlantic from pressure-sensor
544 equipped inverted echo sounders: baroclinic and barotropic components.
545 *J. Atmos. Oceanic Technol.* 26 (12), 2593–2609.

- 546 Behnisch, M., Macrander, A., Boebel, O., Wolff, J.-O., Schörter, J., 2013.
547 Barotropic and deep-referenced baroclinic ssh variability derived from pres-
548 sure inverted echo sounders (pies) south of africa. *J. Geophys. Res.* 118 (6),
549 3046–3058.
550 URL <http://dx.doi.org/10.1002/jgrc.20195>
- 551 Bishop, S. P., Watts, D. R., Donohue, K. A., 2013. Divergent eddy heat
552 fluxes in the Kuroshio Extension at 144°–148°E. Part I: Mean structure.
553 *J. Phys. Oceanogr.* 43 (8), 1533–1550.
- 554 Chang, Y.-L., Oey, L.-Y., 2011. Loop Current Cycle: coupled response of the
555 Loop Current with deep flows. *J. Phys. Oceanogr.* 41 (3), 458–471.
- 556 Chérubin, L. M., Morel, Y., Chassignet, E. P., 2006. Loop Current ring
557 shedding: The formation of cyclones and the effect of topography. *J. Phys.*
558 *Oceanogr.* 36, 569–591.
- 559 Chérubin, L. M., Sturges, W., Chassignet, E. P., 2005. Deep flow variability
560 in the vicinity of the Yucatan Straits from a high-resolution numerical
561 simulation. *J. Geophys. Res.* 110 (C4), C04009.
- 562 Cochrane, J. D., 1972. Separation of an anticyclone and subsequent develop-
563 ments in the Loop Current (1969). *Contributions on the Physical Oceanog-*
564 *raphy of the Gulf of Mexico* 2, 91–106.
- 565 Cronin, M., Watts, D. R., 1996. Eddy-mean flow interaction in the Gulf
566 Stream at 68W. Part I: Eddy energetics. *J. Phys. Oceanogr.* 26, 2107–
567 2131.

- 568 Donohue, K., Watts, D., Hamilton, P., Kennelly, M., Lugo-Fernández, A.,
569 2015. Meanders along the Loop Current Path. *Dynamics of Atmosphere*
570 *and Ocean*. submitted to, this issue.
- 571 Dukhovskoy, D. S., Leben, R. R., Chassignet, E. P., Hall, C. A., Morey,
572 S. L., Nedbor-Gross, R., 2015. Characterization of the uncertainty of Loop
573 Current metrics using a multidecadal numerical simulation and altimeter
574 observations. *Deep Sea Research Part I: Oceanographic Research Papers*
575 100, 140–158.
- 576 Fratantoni, P. S., Lee, T. N., Podesta, G. P., Muller-Karger, F., 1998. The
577 influence of Loop Current perturbations on the formation and evolution of
578 Tortugas eddies in the southern Straits of Florida. *J. Geophys. Res.* 103,
579 24759–24779.
- 580 Griesel, A., Gille, S. T., Sprintall, J., McClean, J. L., Maltrud, M. E., 2009.
581 Assessing eddy heat flux and its parameterization: A wavenumber per-
582 spective from a $1/10^\circ$ ocean simulation. *Ocean Modelling* 29 (4), 248 –
583 260.
- 584 Hamilton, P., 2009. Topographic Rossby waves in the Gulf of Mexico. *Prog.*
585 *Ocean.* 82, 1–31.
- 586 Hamilton, P., Donohue, K., Leben, R. R., Lugo-Fernández, A., Green, R.,
587 2011. Loop Current Observations during Spring and Summer of 2010: De-
588 scription and Historical Perspective. In: Y. Liu, A. MacFadyen, Z.-G. J.,
589 Weisberg, R. (Eds.), *Monitoring and modeling the Deepwater Horizon oil*

- 590 spill: a record-breaking enterprise. Geophysical Monograph 195. American
591 Geophysical Union, Washington DC, pp. 117–130.
- 592 Hamilton, P., Donohue, K. A., Hall, C., Leben, R., Quian, H., Sheinbaum,
593 J., Watts, D., 2014. Observations and Dynamics of the Loop Current,
594 OCS Study BOEM 5015-006, 417 p. New Orleans, LA.
- 595 Hamilton, P., Lugo-Fernández, A., Sheinbaum, A. J., 2015. A Loop Current
596 experiment: Field and remote measurements. Dynamics of Atmosphere
597 and Ocean. submitted to, this issue.
- 598 Howden, S. D., 2000. The three dimensional secondary circulation in devel-
599 oping Gulf Stream meanders. *J. Phys. Oceanogr.* 30, 888–915.
- 600 Huang, H., Walker, N. D., Hsueh, Y., Chao, Y., Leben, R. R., 2013. An
601 analysis of Loop Current frontal eddies in a $\frac{1}{6}^\circ$ Atlantic Ocean model sim-
602 ulation. *J. Phys. Oceanogr.* 43, 1924–1939.
- 603 Hurlburt, H., Thompson, J. D., 1980. A numerical study of Loop Current
604 intrusions and eddy shedding. *J. Phys. Oceanogr.* 10 (10), 1611–1651.
- 605 Hurlburt, H. E., 1986. Dynamic transfer of simulated altimeter data into
606 subsurface information by a numerical ocean model. *J. Geophys. Res.* 91,
607 2372–2400.
- 608 Le Hénaff, M., Kourafalou, V. H., Morel, Y., Srinivasan, A., 2012. Simulating
609 the dynamics and intensification of cyclonic Loop Current Frontal Eddies
610 in the Gulf of Mexico. *J. Geophys. Res.* 117, C02034.

- 611 Leben, R., 2005. Altimeter-derived Loop Current metrics. In: Sturges, W.,
612 Lugo-Fernández, A. (Eds.), *Circulation in the Gulf of Mexico: observations*
613 *and models*. American Geophysical Union, Washington, D.C., pp. 181–202.
- 614 Leben, R. R., Born, G. H., Engebret, B. R., 2002. Operational altimeter
615 data processing for mesoscale monitoring. *Marine Geodesy* 25, 3–18.
- 616 Lindstrom, S. S., Watts, D. R., 1994. Vertical motion in the Gulf Stream
617 near 68°W. *J. Phys. Oceanogr.* 24, 2321–2333.
- 618 Liu, Y., MacFadyen, A., Ji, Z.-G., Weisberg, R. (Eds.), 2011a. Monitoring
619 and modeling the *Deepwater Horizon* oil spill: a record-breaking enterprise.
620 Geophysical Monograph 195. American Geophysical Union, Washington
621 DC.
- 622 Liu, Y., Weisberg, R. H., Hu, C., Kovach, C., Riethmüller, R., 2011b. Evo-
623 lution of the Loop Current System during the *Deepwater Horizon* Oil Spill
624 Event as observed with drifters and satellites. In: Y. Liu, A. MacFadyen,
625 Z.-G. J., Weisberg, R. (Eds.), *Monitoring and modeling the Deepwater*
626 *Horizon* oil spill: a record-breaking enterprise. Geophysical Monograph
627 195. American Geophysical Union, Washington DC, pp. 91–101.
- 628 Marshall, J., Shutts, G., 1981. A note on rotational and divergent eddy fluxes.
629 *J. Phys. Oceanogr.* 11 (12), 1677–1680.
- 630 Meinen, C. S., Watts, D. R., 2000. Vertical structure and transport on a
631 transect across the North Atlantic Current near 42 N: Time series and
632 mean. *J. Geophys. Res.* 105, 21869–21891.

- 633 Nof, D., Pichevin, T., 2001. The ballooning of outflows. *J. Phys. Oceanogr.*
634 31 (10), 3045–3058.
- 635 Oey, L., 2008. Loop current and deep eddies. *J. Phys. Oceanogr.* 38, 1426–
636 1449.
- 637 Oey, L., Lee, H., 2002. Deep eddy energy and topographic Rossby waves in
638 the Gulf of Mexico. *J. Phys. Oceanogr.* 32 (12), 3499–3527.
- 639 Oey, L.-Y., 2004. Vorticity flux through the Yucatan Channel and Loop
640 Current variability in the Gulf of Mexico. *J. Geophys. Res.* 109 (C10),
641 C10004.
- 642 Oey, L.-Y., Lee, H.-C., Schmitz, W. J., 2003. Effects of winds and Caribbean
643 eddies on the frequency of Loop Current eddy shedding: A numerical
644 model study. *J. Geophys. Res.* 108 (C10), 3324.
- 645 Park, J.-H., Watts, D. R., Donohue, K. A., Tracey, K. L., 2012. Compar-
646 isons of sea surface height variability observed by pressure-recording in-
647 verted echo sounders and satellite altimetry in the Kuroshio Extension. *J.*
648 *of Oceanogr.* 68 (3), 401–416.
- 649 Pichevin, T., Nof, D., 1997. The momentum imbalance paradox. *Tellus A*
650 49 (2), 298–319.
- 651 Schmitz, W. J., 2005. Cyclones and westward propagation in the shed-
652 ding of anticyclonic rings from the Loop Current. In: Sturges, W., Lugo-
653 Fernández, A. (Eds.), *Circulation in the Gulf of Mexico: observations and*
654 *models*. American Geophysical Union, Washington, D.C., pp. 241–261.

- 655 Shay, L. K., Jaimes, B., Brewster, J. K., Meyers, P., McCaskill, E. C.,
656 Uhlhorn, E., Marks, F., Halliwell Jr, G. R., Smedstad, O. M., Hogan, P.,
657 2011. Airborne ocean surveys of the Loop Current complex from NOAA
658 WP-3D in support of the *Deepwater Horizon* oil spill. In: Y. Liu, A. Mac-
659 Fadyen, Z.-G. J., Weisberg, R. (Eds.), Monitoring and modeling the *Deep-*
660 *water Horizon* oil spill: a record-breaking enterprise. Geophysical Mono-
661 graph 195. American Geophysical Union, Washington DC, pp. 131–151.
- 662 Sturges, W., Leben, R., 2000. Frequency of ring separations from the Loop
663 Current in the Gulf of Mexico: A revised estimate. *J. Phys. Oceanogr.*
664 30 (7), 1814–1819.
- 665 Vukovich, F. M., Maul, G. A., 1985. Cyclonic eddies in the eastern Gulf of
666 Mexico. *J. Phys. Oceanogr.* 15, 105–117.
- 667 Walker, N., Pilley, C., Raghunathan, V., D’Sa, E., Leben, R., Hoffman, N.,
668 Brickley, P., Coholan, P., Sharma, N., Graber, H., Turner, R., 2011. Im-
669 pacts of Loop Current frontal cyclonic eddies and wind forcing on the 2010
670 Gulf of Mexico oil spill. In: Y. Liu, A. MacFadyen, Z.-G. J., Weisberg, R.
671 (Eds.), Monitoring and modeling the *Deepwater Horizon* oil spill: a record-
672 breaking enterprise. Geophysical Monograph 195. American Geophysical
673 Union, Washington DC, pp. 103–116.
- 674 Welch, P. D., 1967. The use of the fast Fourier transform for the estimation
675 of power spectra: A method based on time averaging over short, modified
676 periodograms. *IEEE Trans. Audio Electroacoustics* AU-15 (2), 70–73.

677 Welsh, S. E., Inoue, M., 2000. Loop Current rings and the deep circulation
678 in the Gulf of Mexico. *J. Geophys. Res.* 105 (C7), 16951–16959.

679 Zavala-Hidalgo, J., Morey, S. L., O'Brien, J. J., 2003. Cyclonic eddies north-
680 east of the Campeche Bank from altimetry data. *J. Phys. Oceanogr.* 33,
681 623–629.

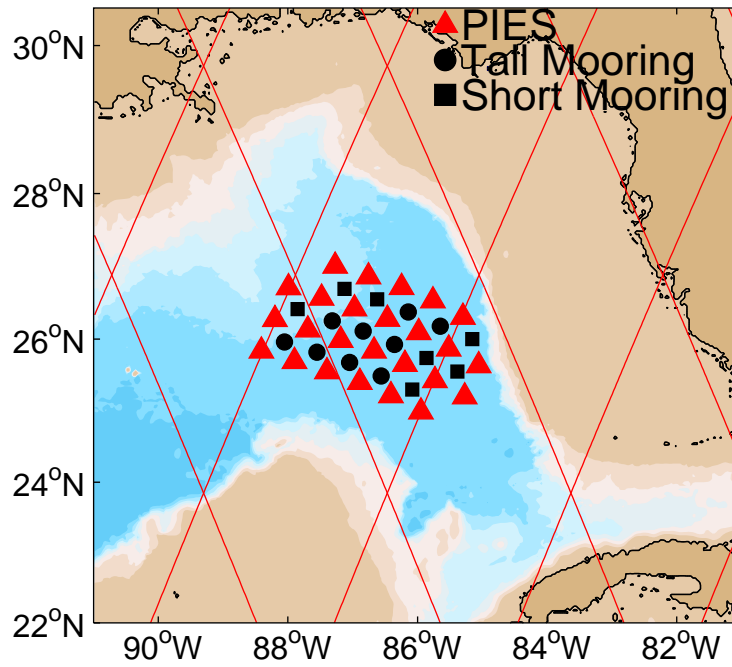


Figure 1: Dynamics of the Loop Current Array consisted of 25 pressure inverted echo sounders, PIES, (red triangle), 9 tall moorings (black circles) and 7 short moorings (black squares). Bathymetry contoured every 1000 m depth, deepest topography denoted by the darkest blue hues. Jason-2 altimetry tracks shown in red.

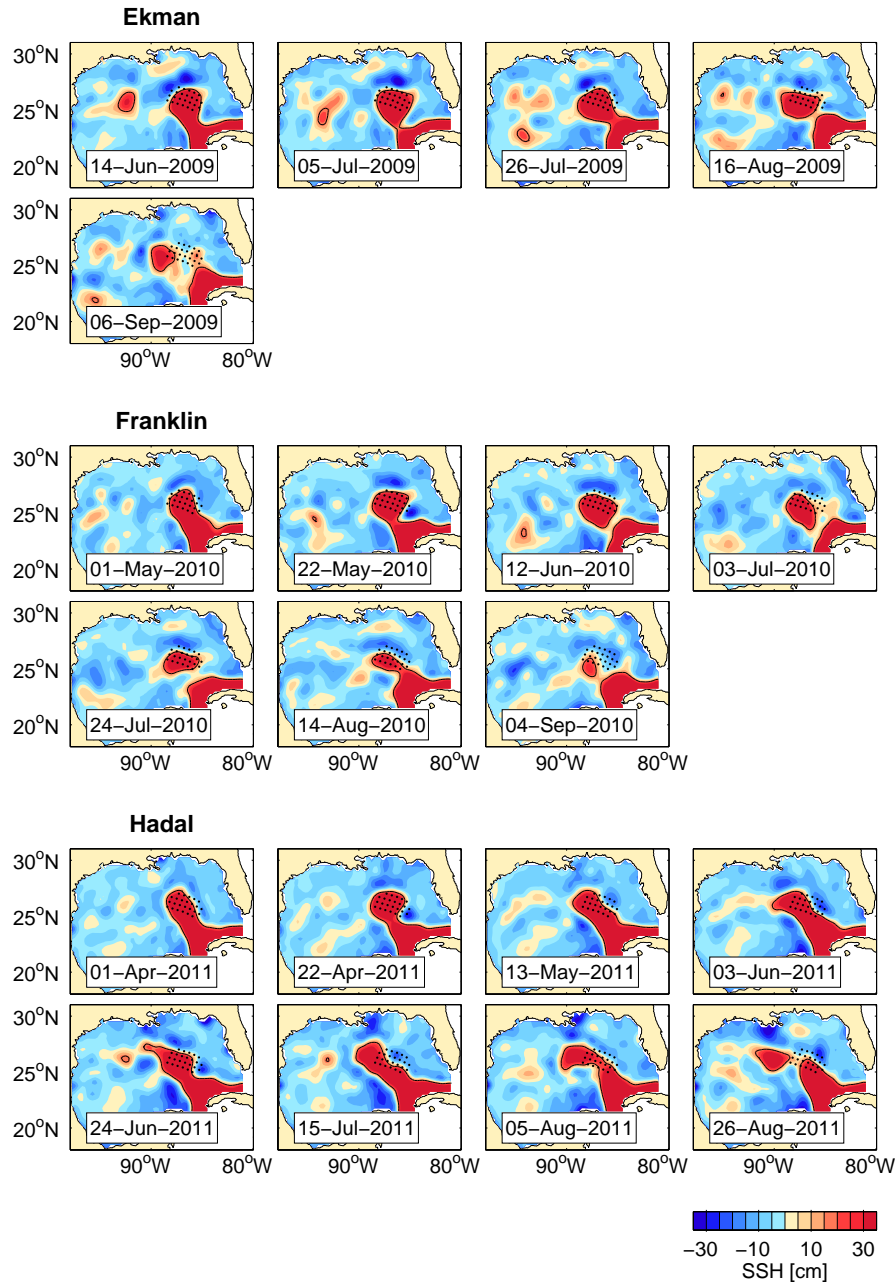


Figure 2: Sea surface height fields at 21-day intervals during the three Loop Current Eddy separations which occurred during the Dynamics of the Loop Current experiment. PIES locations are shown as black dots in each panel. Mapped SSH determined from the Colorado Center for Atmospheric Research (CCAR) Gulf of Mexico objectively mapped historical mesoscale altimeter data reanalysis. Date noted in the lower left of each panel. SSH contour interval is 5 cm.

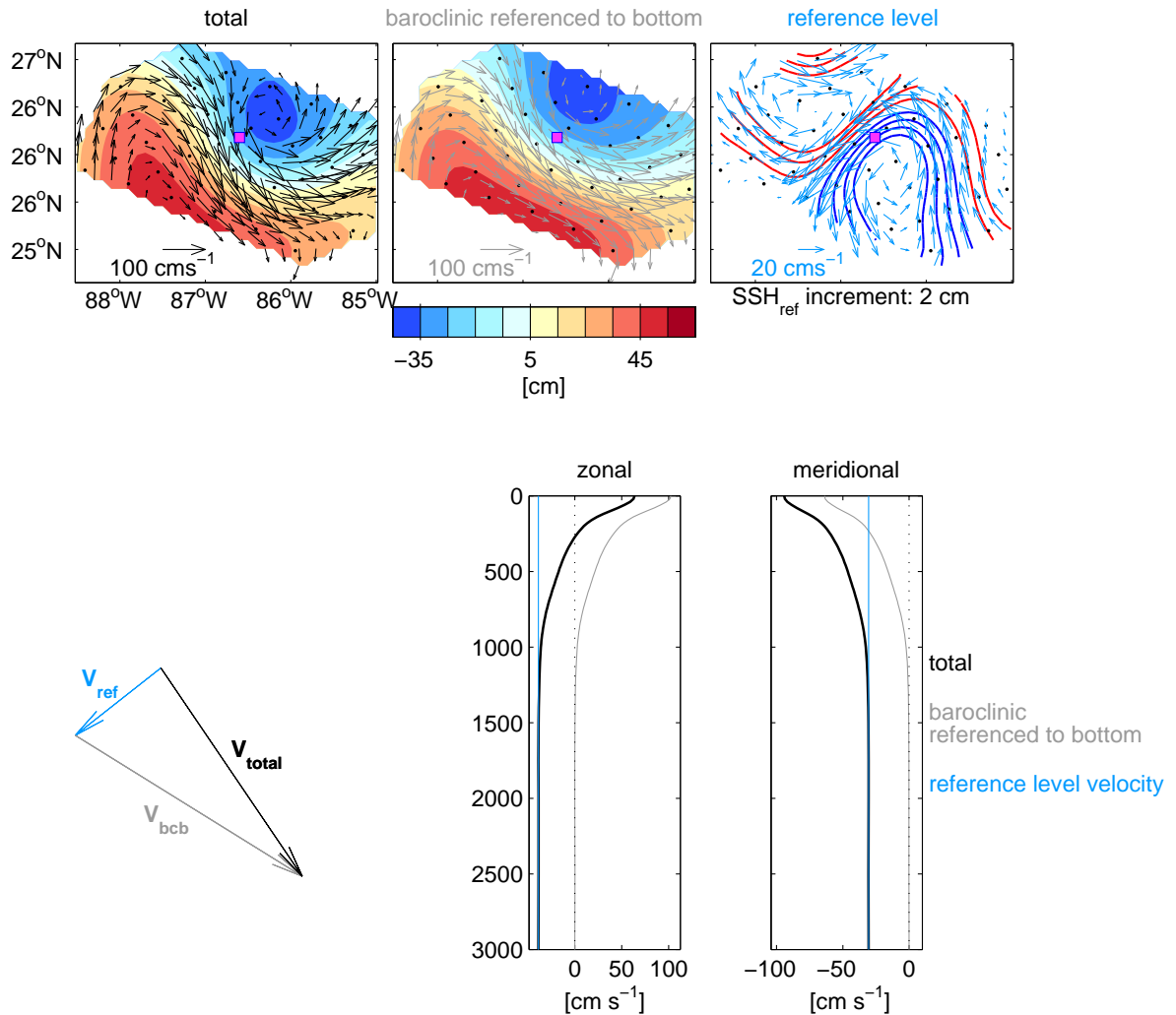


Figure 3: Several views of the circulation on June 24, 2010 provided by the PIES and current meter measurements. Top panels: Total sea surface height in plan view (left), displaying its baroclinic contribution referenced to the bottom (middle) and reference level contribution (right). Anticyclonic circulations shown by reddish hues; cyclonic circulations by bluish hues. Mapped current vectors plotted at 20 km spacing. PIES and current meter sites denoted by black circles. Bottom left panel: The vector sum of deep reference velocity (blue arrow) and baroclinic referenced to the bottom velocity (gray arrow) produces the total velocity. A baroclinic velocity profile that is vertically aligned like this is called equivalent barotropic. Bottom two right panels: Zonal and meridional velocity (total is black, reference level velocity is blue, and baroclinic referenced to the bottom is gray) at the magenta square shown in the upper panels.

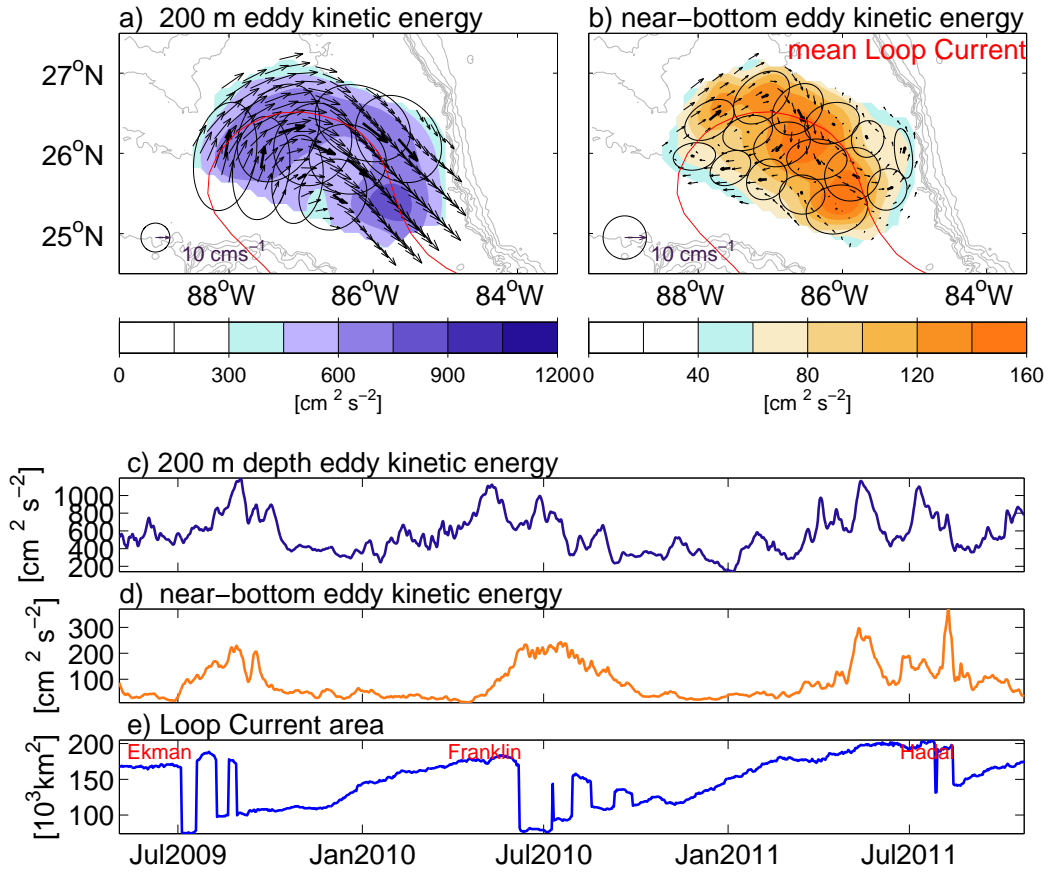


Figure 4: Mapped and directly measured mean currents (respectively thin and bold vectors) for 200 m level (panel a) and near bottom (panel b). Standard deviation ellipses superimposed on the time-mean eddy kinetic energy (color-bar, $\text{cm}^2 \text{s}^{-2}$). Scale for vectors and ellipses shown in lower left corner. Red line denotes the mean Loop Current position defined by the CCAR-SSH 17 cm contour. Bathymetry plotted with gray contours every 500 m depth. Time mean is taken over the 30-month experiment duration from May 3, 2009 through October 23, 2011. Panels c and d: Time series of array-averaged 200 m (panel c) and near-bottom (panel d) eddy kinetic energy in units of $\text{cm}^2 \text{s}^{-2}$. Panel e: Time series of array-average CCAR-SSH derived Loop Current area in units of 10^3km^2 .

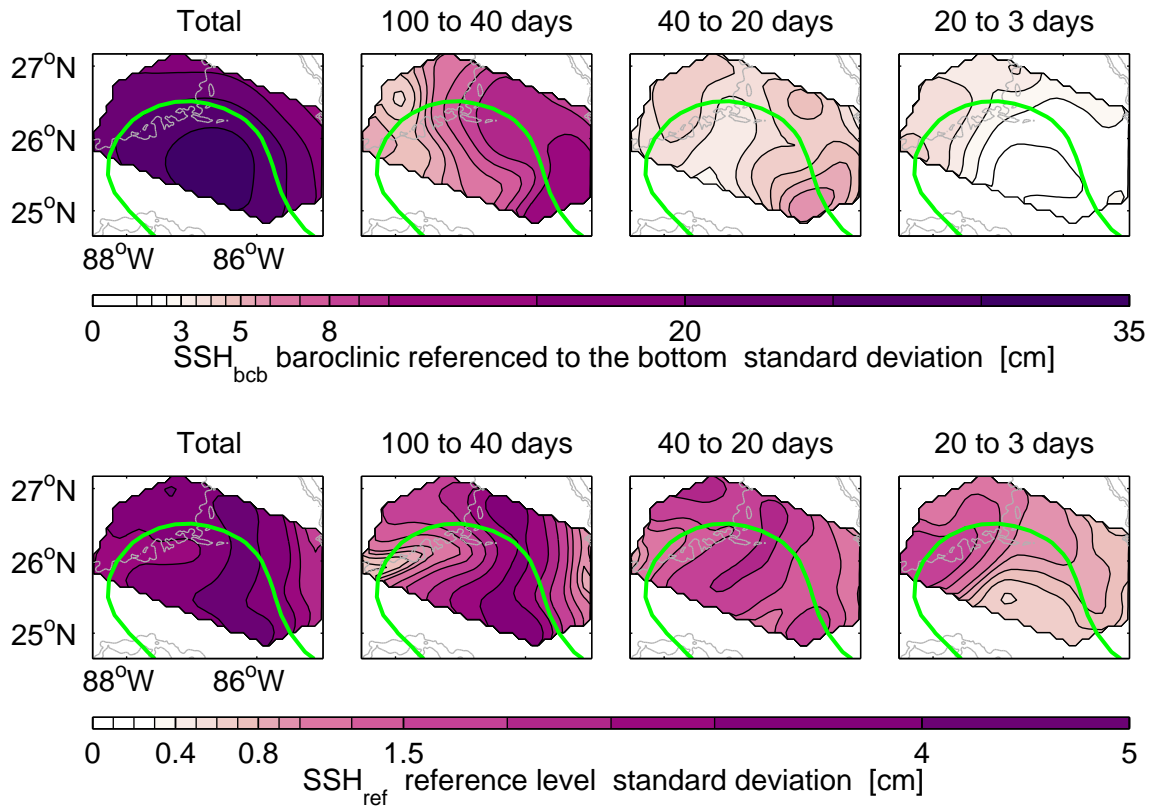


Figure 5: Standard deviation of SSH_{bcb} (top panels) and SSH_{ref} (bottom panels) as a function of frequency band. Leftmost panels show total standard deviation. Three right panels: Standard deviation in three frequency bands noted above each panel. Bathymetry contoured in gray every 500 m depth. Note that the colorbar contour interval is not uniform.

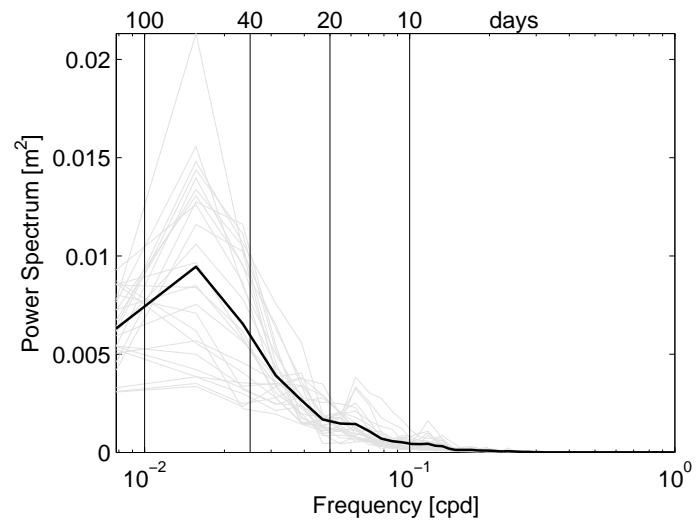


Figure 6: Variance-preserving power spectrum for individual (gray) and array-averaged (black) PIES SSH_{bcb} . Frequency limits that define the frequency bands evaluated in Figure 5 are denoted with vertical black lines.

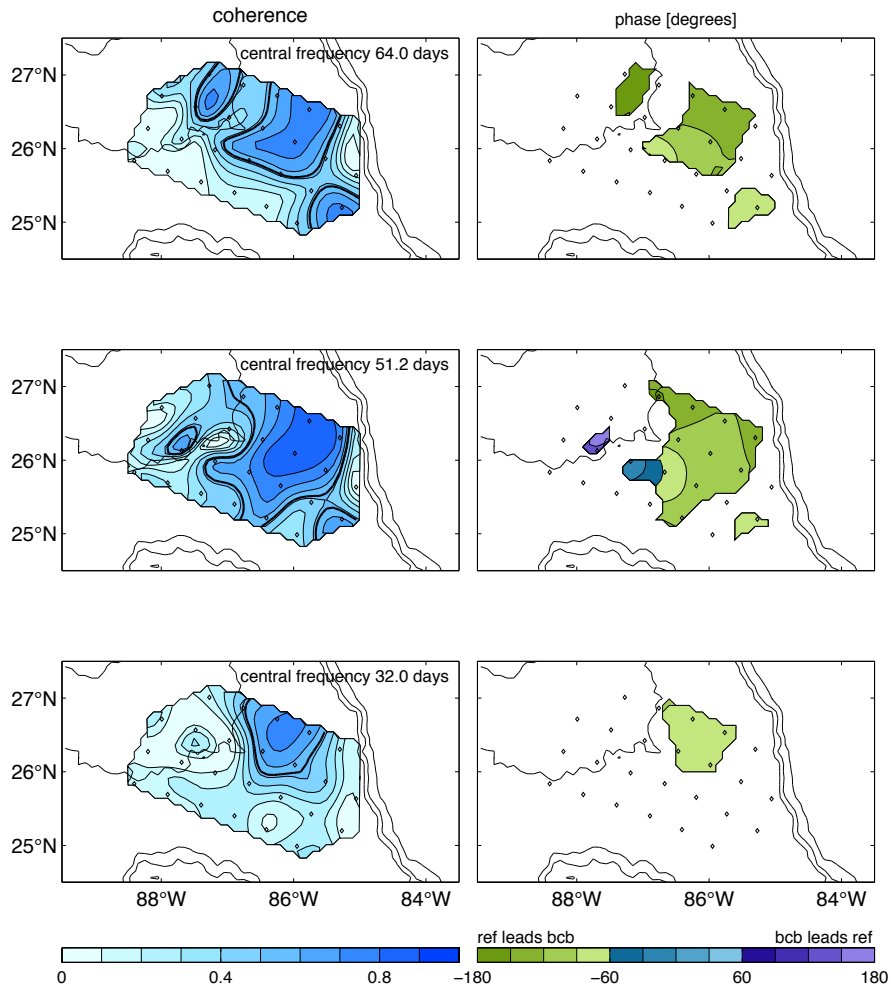


Figure 7: Coherence (left) and phase (right) between upper, SSH_{bc} , and lower, SSH_{ref} , streamfunction for three frequency bands: top ($1/64 \text{ d}^{-1}$), middle ($1/51.2 \text{ d}^{-1}$), and bottom ($1/32 \text{ d}^{-1}$), estimated using Welch's averaged periodogram method (256-day length segment with 50% overlap). Phase (in degrees) contoured where coherence exceeds 95% confidence limits denoted by the thick black contour in the coherence maps. Negative phase indicates that deep leads upper. PIES locations shown by black diamonds. Bathymetry (thin black line) contoured every 1000 m depth.

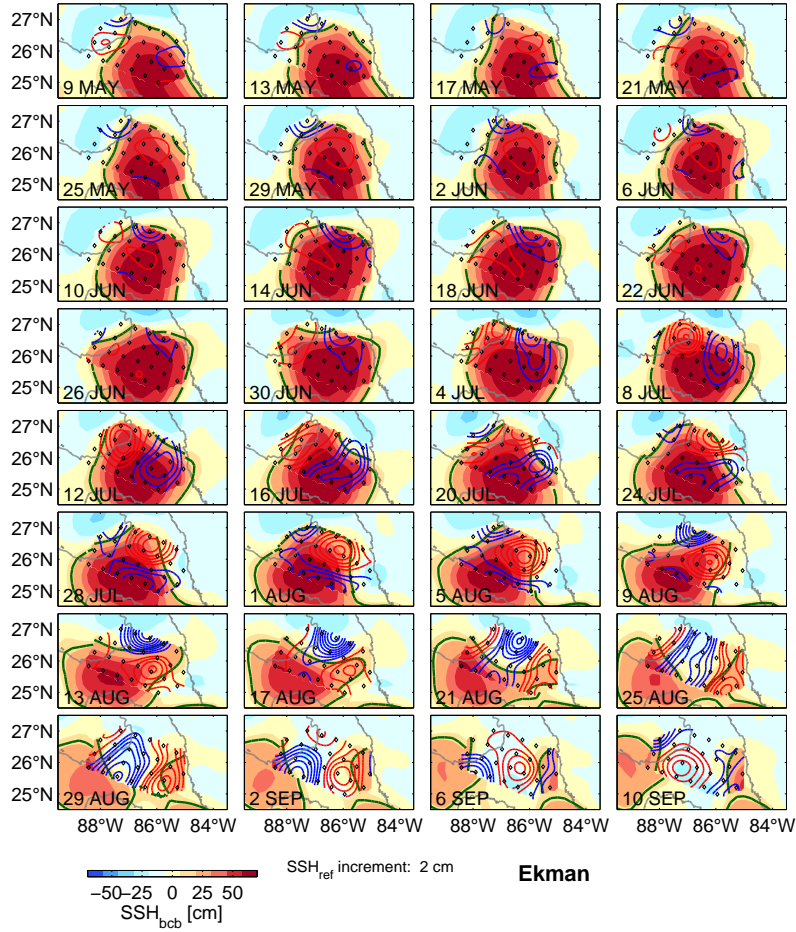


Figure 8: Loop Current Eddy shedding event Ekman May 9 through September 10 2009. Maps of baroclinic SSH referenced to the bottom (SSH_{bcb}) embedded within altimetric SSH (filled color contours; colorbar and contour interval in the bottom left figure corner). Maps shown sequentially left to right, top to bottom at 4-day intervals. The 17 cm contour (bold green, SSH_{bcb} within array, altimetric SSH outside array) denotes the location of the Loop Current. Mapped reference level SSH (SSH_{ref}) reveals the presence of deep cyclones (thin blue contours) and anticyclones (thin red contours) contoured every 2 cm. Diamonds denote PIES sites. Gray lines denote the 3000 m depth contour.

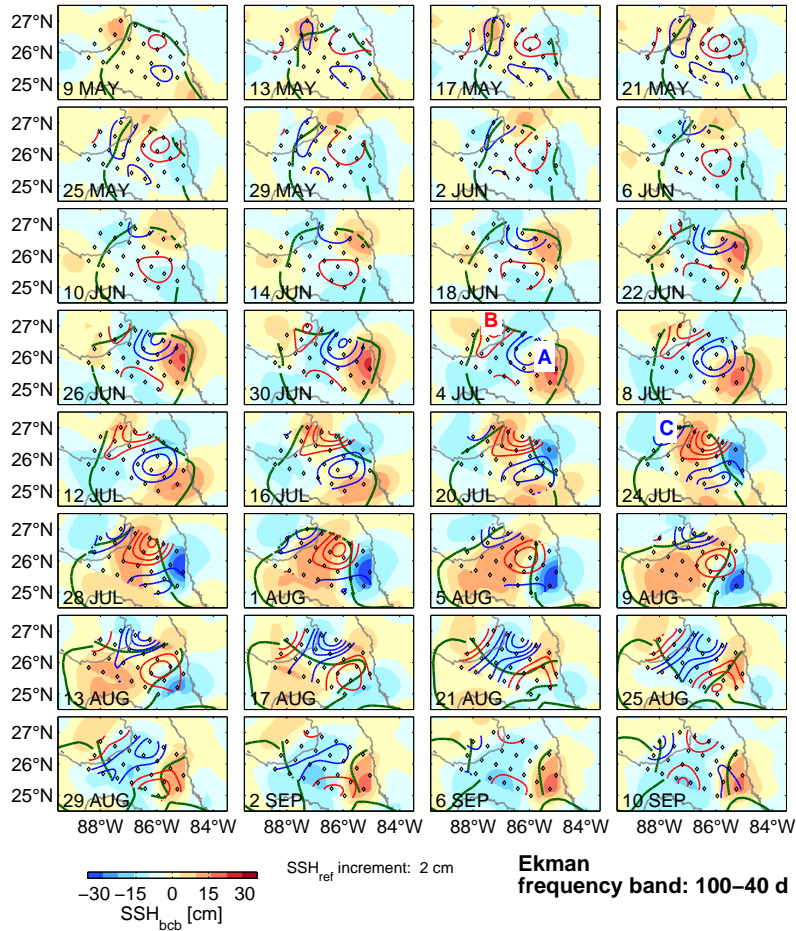


Figure 9: Loop Current Eddy shedding event Ekman May 9 through September 10 2009. Maps of 100-40 day band-passed baroclinic SSH referenced to the bottom (SSH_{bcb}) embedded within altimetric SSH (filled color contours; colorbar and contour interval in the bottom left figure corner). Maps shown sequentially left to right, top to bottom at 4 day intervals. The 17 cm contour (bold green, SSH_{bcb} within array, altimetric SSH outside array) denotes the location of the Loop Current. Mapped 100-40 day band-passed reference level SSH (SSH_{ref}) reveals the presence of deep cyclones (thin blue contours) and anticyclones (thin red contours) contoured every 2 cm. Diamonds denote PIES sites. Gray lines denote the 3000 m depth contour. The July 4 map indicates deep cyclone A and deep anticyclone B discussed in the text. The July 24 map indicates deep cyclone C discussed in the text.

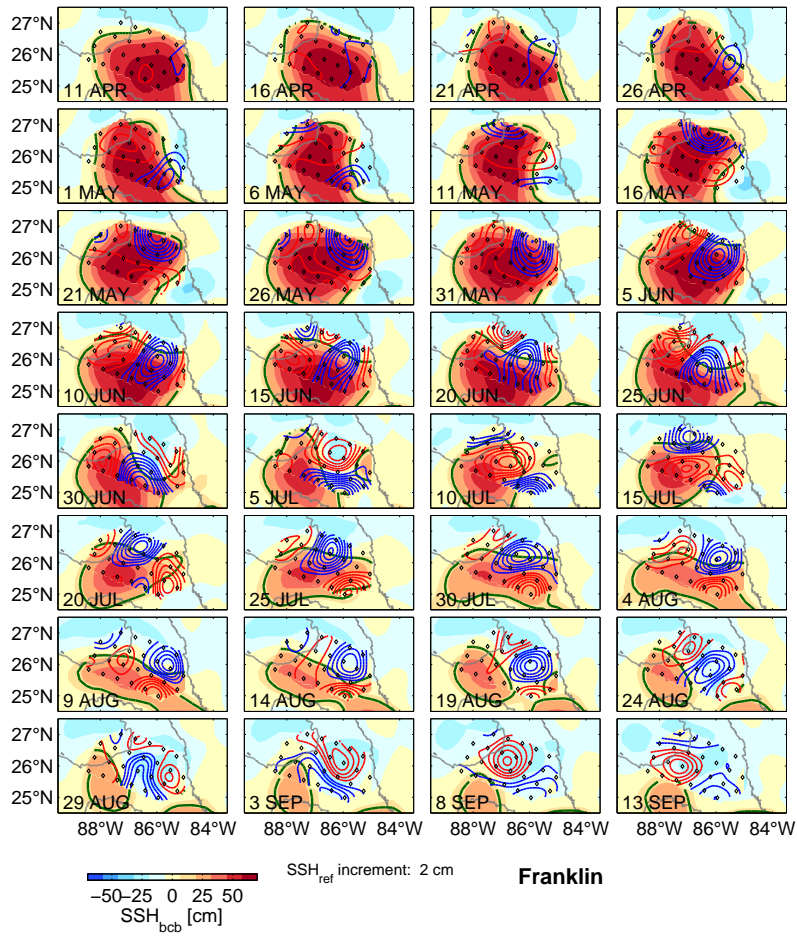


Figure 10: Same as Figure 8, for Loop Current Eddy shedding event Franklin April 11 through September 13, 2010.

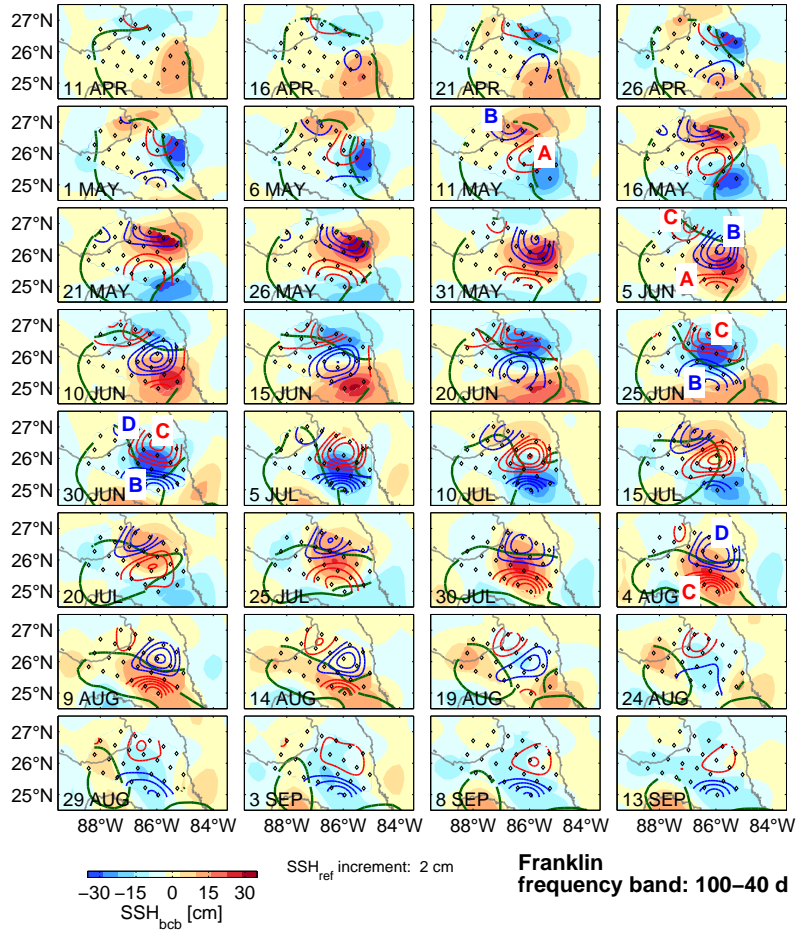


Figure 11: Same as Figure 9, for Loop Current Eddy shedding event Franklin April 11 through September 13, 2010. The May 11 map indicates deep anticyclone A and deep cyclone B discussed in the text. The June 5 map indicates deep anticyclone C discussed in the text. The June 30 map indicates deep cyclones B, D and deep anticyclone C discussed in the text. The August 4 map also indicates deep cyclone D and deep anticyclone C.

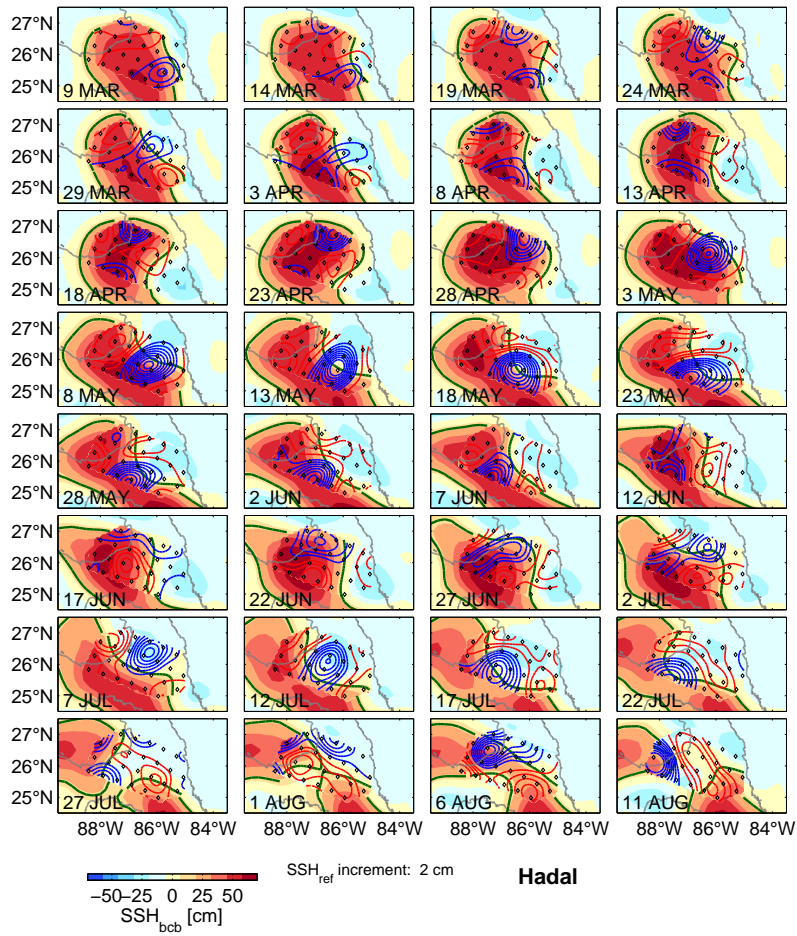


Figure 12: Same as Figure 8, Loop Current Eddy shedding event Hadal March 9 through August 11, 2011.

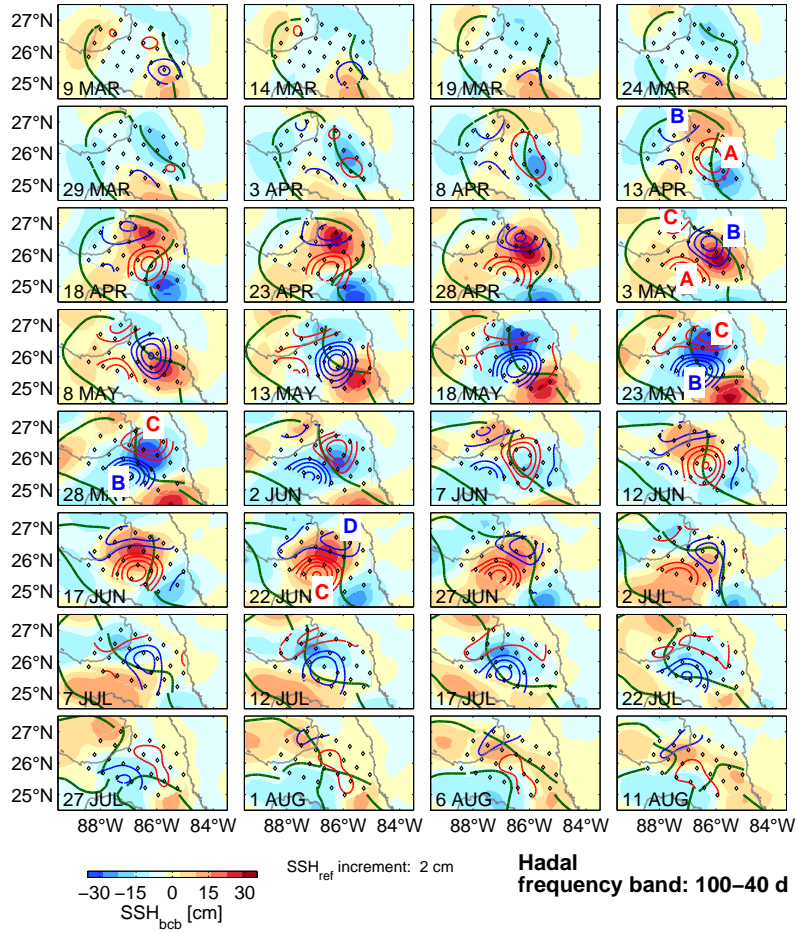


Figure 13: Same as Figure 9, Loop Current Eddy shedding event Hadal March 9 through August 11, 2011. The April 13, May 3 and May 23 maps indicate deep anticyclone A, deep cyclone B, and deep anticyclone C, respectively. The May 28 map indicates deep cyclone B and deep anticyclone C discussed in the text. The June 22 map indicates the deep cyclone D discussed in the text.

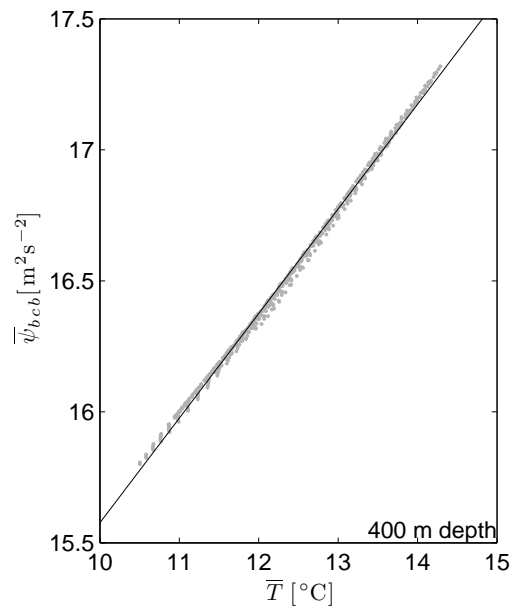


Figure 14: A nearly linear relationship (black line) exists between between mean ψ_{bcb} and mean T at 400 m (gray dots).

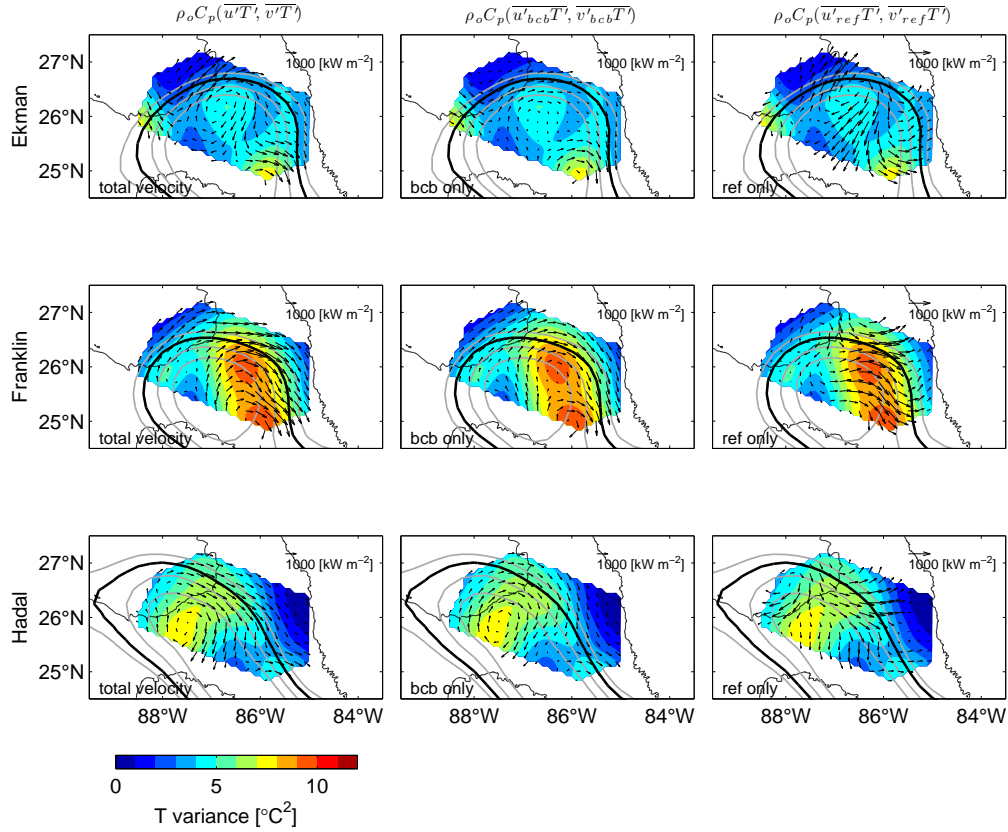


Figure 15: Eddy heat flux vectors at 400 m depth for the three Loop Current Eddy shedding events superimposed on the 400 m depth temperature variance (same across each row). Rows correspond to time averages over the Loop Current Eddy shedding events: Ekman May 3 through August 31, 2009 (top), Franklin February 15 through September 14, 2010 (middle), Hadal March 1 through September 14, 2011 (bottom). Columns correspond to the perturbation velocity used in the eddy heat flux calculation: total (left), baroclinic-referenced-to-the-bottom (center), reference (right). The bold black line denotes the mean position of the 17 cm altimeter-mapped SSH contour; gray contours indicate the 10, 27, and 37 cm contour. The 3000 m isobath contoured with thin black line.

Ekman May.03,2009 through Aug.31,2009 400 m depth

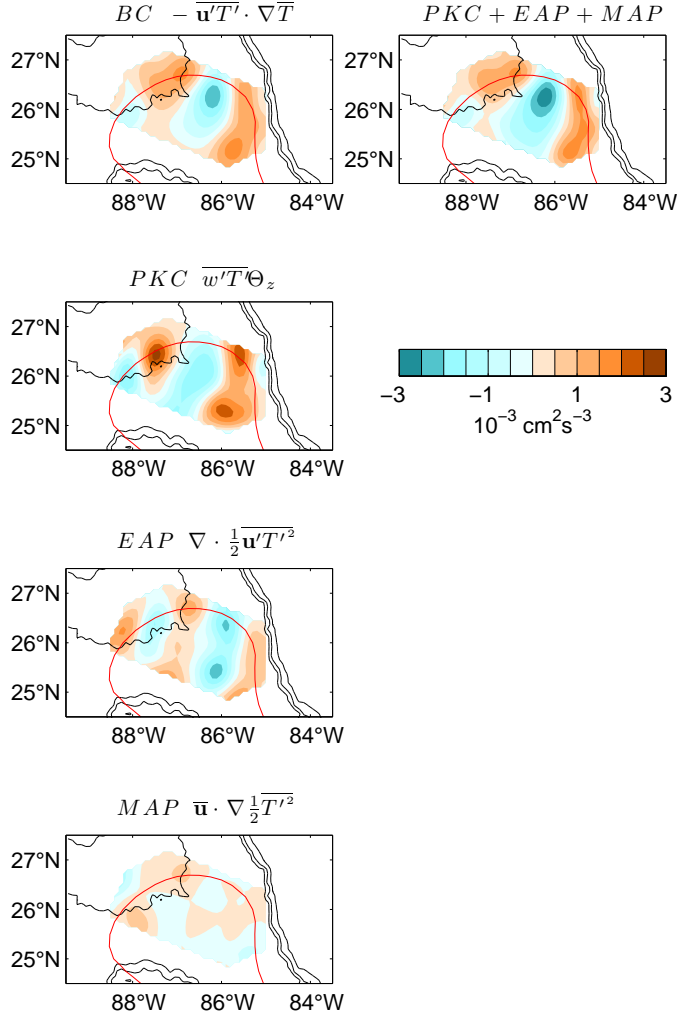


Figure 16: Four terms in the steady eddy potential energy budget (Eqn 15) determined for the Ekman event May 3 through August 31, 2009 at 400 m depth (contour interval after multiplication by $g\alpha/\Theta_z = 428 \text{ cm}^2\text{s}^{-2}\text{C}^{-2}$ is $0.5 \times 10^{-3} \text{ cm}^2 \text{ s}^{-3}$; in colorbar blues hues are negative and orange hues are positive). The horizontal downgradient eddy heat flux (BC) is balanced by the mean advection of eddy potential energy (MAP), eddy advection of eddy potential energy (EAP) and the vertical downgradient heat flux (PKC). Right panel shows the sum of the PKC, EAP and MAP terms. The red line denotes the mean position of the 17 cm altimeter-mapped SSH contour. Bathymetry (thick black lines) contoured every 1000 m depth.

Ekman May.03,2009 through Aug.31,2009 400 m depth

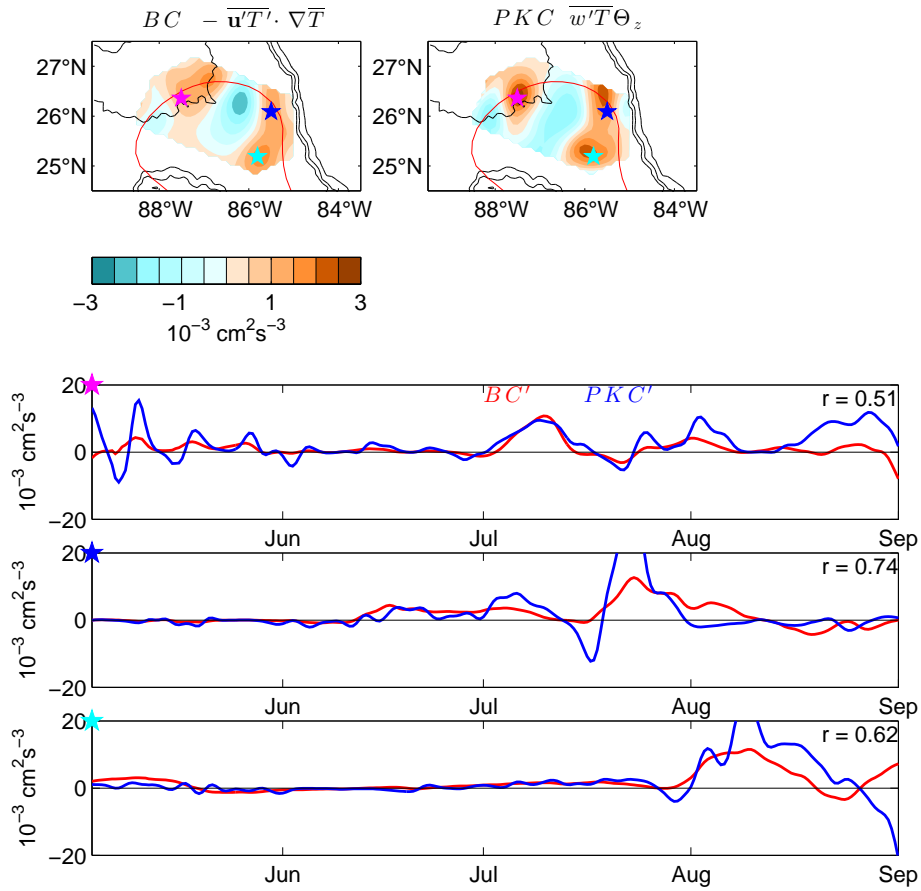


Figure 17: Top panels: BC (left) and PKC (right) at 400 m depth determined for the Ekman event (contour interval after multiplication by $g\alpha/\Theta_z = 428 \text{ cm}^2\text{s}^{-2}\text{C}^{-2}$ is $0.5 \times 10^{-3}\text{cm}^2 \text{ s}^{-3}$; in colorbar blues hues are negative and orange hues are positive). The red line denotes the mean position of the 17 cm altimeter-mapped SSH contour. Bathymetry (thick black lines) contoured every 1000 m depth. Bottom three panels: time series of BC' (red) and PKC' (blue) at locations indicated by colored stars in the mapped energetic terms (top panels) and denoted on the top left corner of each time series plot.

Franklin Feb.15,2010 through Sep.14,2010 400 m depth

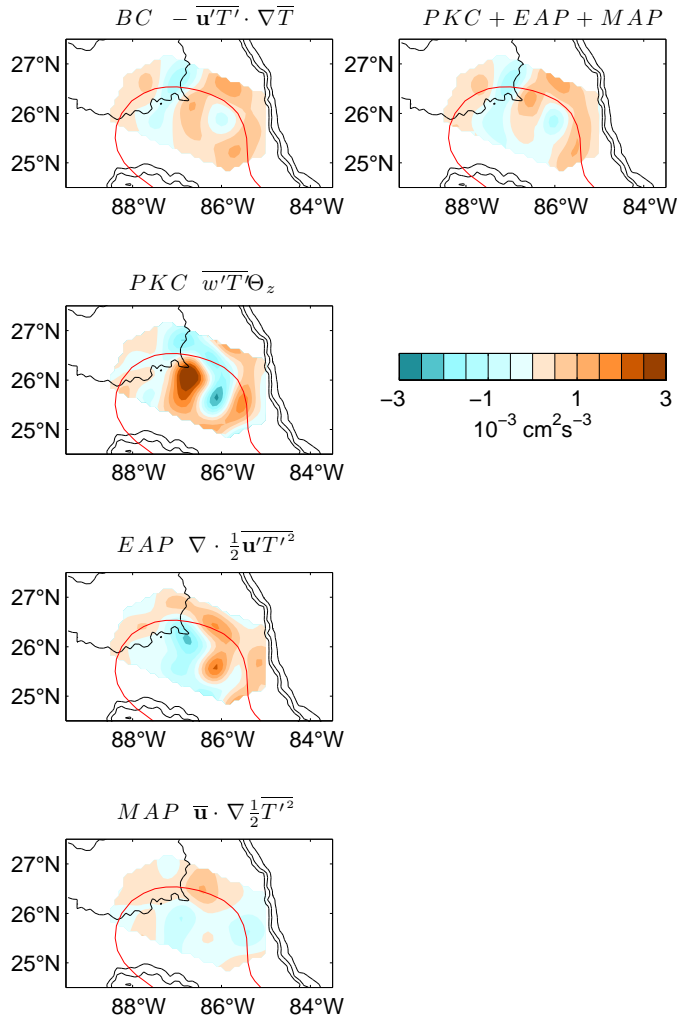


Figure 18: Four terms in the steady eddy potential energy budget (Eqn 15) determined for the Franklin event February 15 through September 14, 2010 at 400 m depth (contour interval after multiplication by $g\alpha/\Theta_z = 428 \text{ cm}^2 \text{ s}^{-2} \text{ C}^{-2}$ is $0.5 \times 10^{-3} \text{ cm}^2 \text{ s}^{-3}$; in color-bar blues hues are negative and orange hues are positive). The horizontal downgradient eddy heat flux (BC) is balanced by the mean advection of eddy potential energy (MAP), eddy advection of eddy potential energy (EAP) and the vertical downgradient heat flux (PKC). Right panel shows the sum of the PKC, EAP and MAP terms. The red line denotes the mean position of the 17 cm altimeter-mapped SSH contour. Bathymetry (thick black lines) contoured every 1000 m depth. 50

Franklin Feb.15,2010 through Sep.14,2010 400 m depth

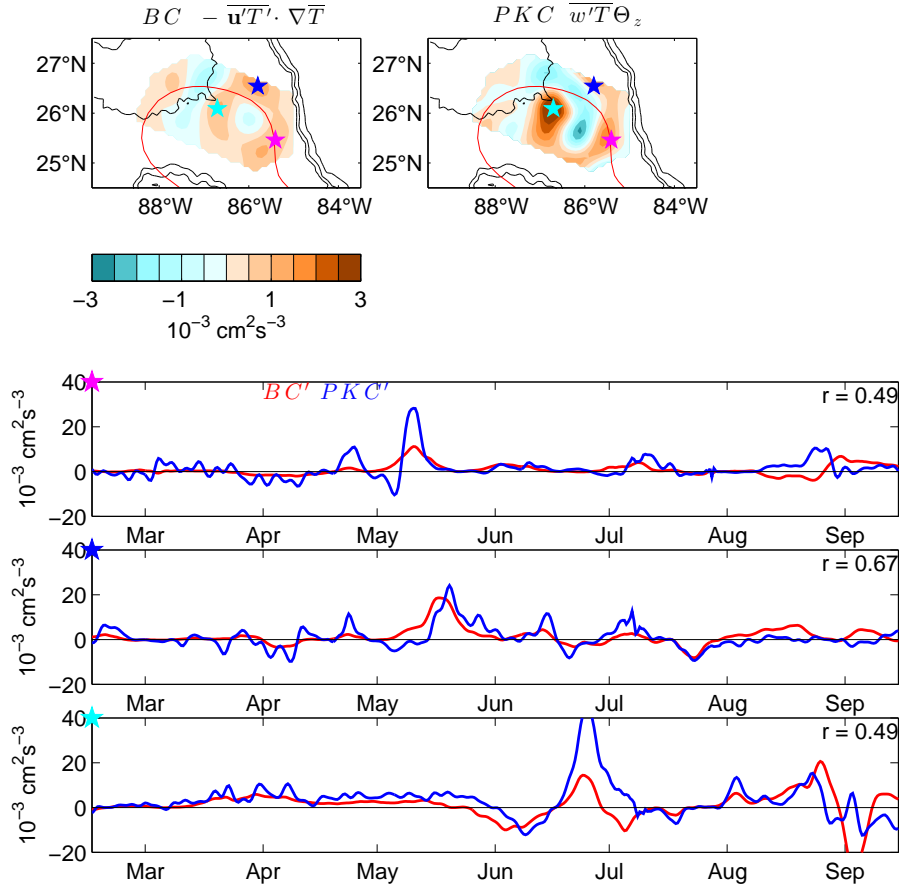


Figure 19: Top panels: BC (left) and PKC (right) at 400 m depth determined for the Franklin event (contour interval after multiplication by $g\alpha/\Theta_z = 428 \text{ cm}^2\text{s}^{-2}\text{C}^{-2}$ is $0.5 \times 10^{-3}\text{cm}^2 \text{ s}^{-3}$; in colorbar blues hues are negative and orange hues are positive). The red line denotes the mean position of the 17 cm altimeter-mapped SSH contour. Bathymetry (thick black lines) contoured every 1000 m depth. Bottom three panels: time series of BC' (red) and PKC' (blue) at locations indicated by colored stars in the mapped energetic terms (top panels) and denoted on the top left corner of each time series plot.

Hadal Mar.01,2011 through Sep.14,2011 400 m depth

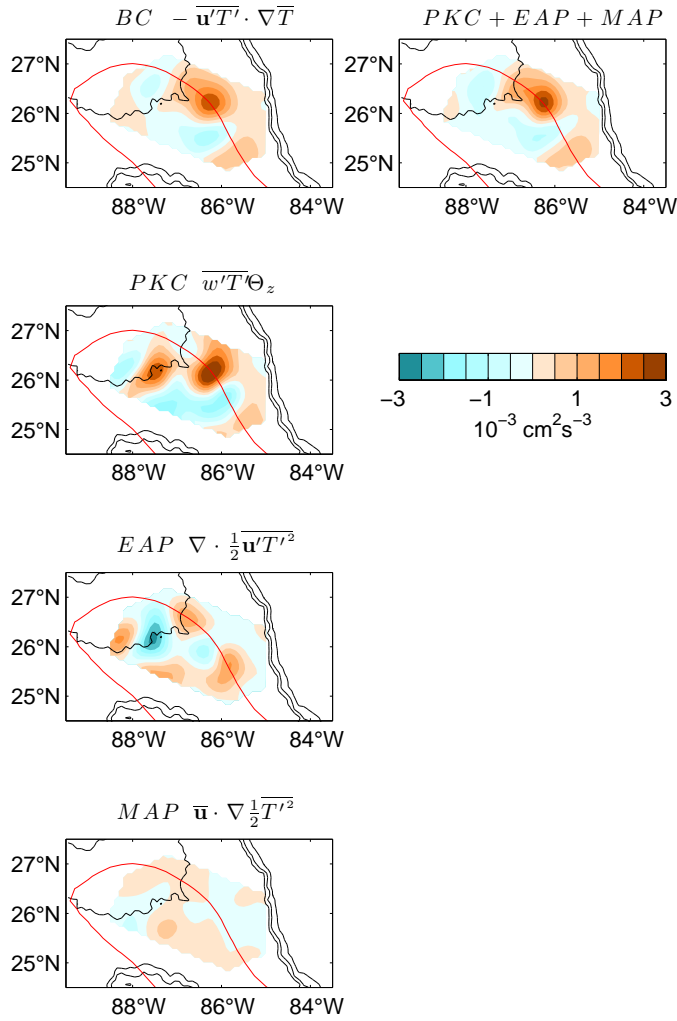


Figure 20: Four terms in the steady eddy potential energy budget (Eqn15) determined for the Hadal event March 1 through September 14, 2011, at 400 m depth (contour interval after multiplication by $g\alpha/\Theta_z = 428 \text{ cm}^2\text{s}^{-2}\text{C}^{-2}$ is $0.5 \times 10^{-3} \text{ cm}^2 \text{ s}^{-3}$; in colorbar indicates blues hues are negative and orange hues are positive). The horizontal downgradient eddy heat flux (BC) is balanced by the mean advection of eddy potential energy (MAP), eddy advection of eddy potential energy (EAP) and the vertical downgradient heat flux (PKC). Right panel shows the sum of the PKC, EAP and MAP terms. The red line denotes the mean position of the 17 cm altimeter-mapped SSH contour. Bathymetry (thick black lines) contoured every 1000 m depth. 52

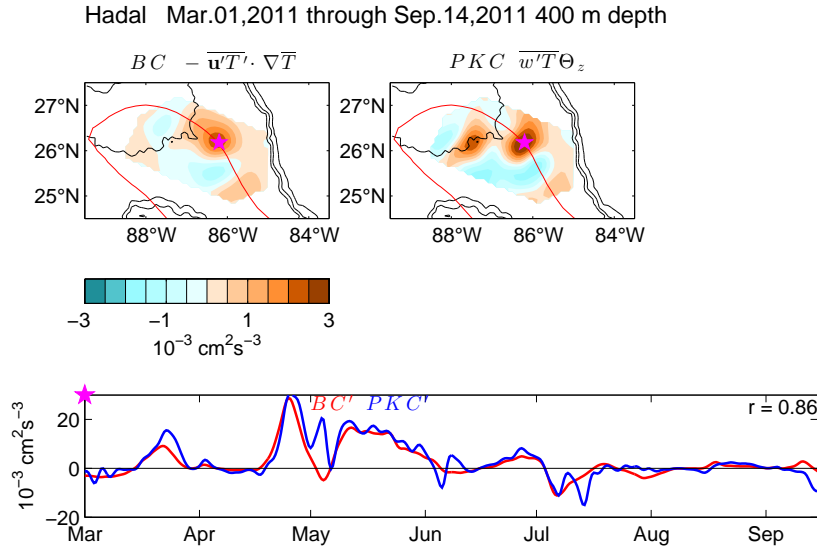


Figure 21: Top panels: BC (left) and PKC (right) at 400 m depth determined for the Hadal event (contour interval after multiplication by $g\alpha/\Theta_z = 428 \text{ cm}^2\text{s}^{-2}\text{C}^{-2}$ is $0.5 \times 10^{-3} \text{ cm}^2 \text{ s}^{-3}$; in colorbar blues hues are negative and orange hues are positive). The red line denotes the mean position of the 17 cm altimeter-mapped SSH contour. Bathymetry (thick black lines) contoured every 1000 m depth. Bottom three panels: time series of BC' (red) and PKC' (blue) at locations indicated by colored stars in the mapped energetic terms (top panels) and denoted on the top left corner of each time series plot.